In-situ full-field mapping of melt flow dynamics in laser metal additive manufacturing

Qilin Guo [a, b], Cang Zhao [c], Minglei Qu [a, b], Lianghua Xiong [b], S. Mohammad H. Hojjatzadeh [a, b], Luis I. Escano [a, b], Niranjan D. Parab [c], Kamel Fezzaa [c], Tao Sun [c, *], Lianyi Chen [a, b, **]

[a] Department of Mechanical Engineering, University of Wisconsin-Madison, Madison, WI 53706, USA

[b] Department of Mechanical and Aerospace Engineering, Missouri University of Science and Technology, Rolla, MO 65409, USA

[c] X-ray Science Division, Advanced Photon Source, Argonne National Laboratory, Lemont, IL 60439, USA

* Corresponding author

** Corresponding author

E-mail addresses: lianyi.chen@wisc.edu (Lianyi Chen), taosun@aps.anl.gov (Tao Sun)

Abstract

Melt flow plays a critical role in laser metal additive manufacturing, yet the melt flow behavior within the melt pool has never been explicitly presented. Here, we report in-situ characterization of melt-flow dynamics in every location of the entire melt pool in laser metal additive manufacturing by populous and uniformly dispersed micro-tracers through in-situ high-resolution synchrotron x-ray imaging. The location-specific flow patterns in different regions of the melt pool are revealed and quantified under both conduction mode and depression mode. The physical processes at different locations in the melt pool are identified. The full-field melt-flow mapping approach reported here opens the way to study the detailed melt-flow dynamics under real additive manufacturing conditions. The results obtained provide crucial insights into laser additive manufacturing processes and are critical for developing reliable high-fidelity computational models.

Keywords: Metal additive manufacturing, powder bed fusion, laser processing, melt flow, x-ray imaging

1. Introduction

Melt flow within the melt pool in laser metal additive manufacturing [e.g., laser powder bed fusion (LPBF), direct energy deposition (DED)] determines the heat transfer and mass transfer, thus plays a critical role in melt pool development [1], defect formation and evolution [2–8], solidification [9–11], and spatter generation [12–14]. Consequently, the melt flow behavior significantly affects the microstructures and properties of the additively manufactured parts [4,5,15–17]. Therefore, understanding the melt flow behavior in the melt pool is crucial for microstructure prediction and process control.

Due to the difficulty in experimentally visualizing the fluid flow inside the melt pool, extensive modelling and simulation work have been carried out to study the flow patterns under various conditions, i.e., with different laser power and scan speed that favors either depression-mode melting (a depression is formed in the melt pool under high power density due to the recoil pressure that caused by the intense material vaporization) or conduction-mode melting (a relatively shallow and wide melt pool is created under low power density without having a visible depression) [15,18]. Effect of surface active agent on melt flow was also studied by simulation [19]. However, given the complexity of the physics in laser additive manufacturing, it is extremely challenging to simulate the involved multi-physics phenomena using a single numerical model [20]. In fact, major assumptions must be applied in most of simulations [7,15,19–25]: some of assumptions are applied for the sake of calculation efficiency, some are made due to the unavailability of data, and the others are made because the underlying physics are still not well understood. All these assumptions will affect the accuracy of the models to certain extent. As a result, even though most of the models have been validated by comparing the simulated melt pool/track shape or size with post-mortem characterization results, the calculated melt flow results are not always consistent, and sometimes are even opposite. Discrepancies of the flow prediction were observed along the front depression wall [10,26,27], along the rear depression wall [13,18], along the bottom of melt pool [13,28], around the depression outlet [10,29], and behind the depression outlet [26,28]. Moreover, some physical mechanisms during laser processing under depression mode were interpreted with the more computation-efficient conduction-mode model, regardless of the essential distinction between the two melting modes. Thus, it is critical to experimentally unveil the melt flow behavior within the melt pool in laser additive manufacturing under both conduction-mode and depression-mode melting, for understanding the actual melt flow behavior and for developing and validating computational models.

Extensive work has been done in the welding community to characterize the liquid flow behavior in the melt pool by using flow tracers in the last few decades [3,4,12,14,16,26,30–37]. A very recent paper provides direct evidence of surface active element induced flow pattern reversion [38]. The tracers used in welding research are usually in relatively large size (50 µm – 500 µm) and small amount (≤ 80 counts per test), which can only trace melt flow behavior in certain area of the melt pool. Visible light imaging, such as glass flanking [4,35], were used to directly observe the flow pattern inside melt pool. However, the glass plate changes the heat transfer condition and cuts off the flow at the cross section, so that the observed flow pattern may differ from the real laser processing condition. Recently, in-situ x-ray imaging was used to study laser additive manufacturing processes [39–49]. The latest research [8] used tungsten particles to trace melt flow by synchrotron x-ray imaging, but only presented melt flow behavior in one projected view and in localized area of the melt pool.

Characterizing the three-dimensional melt flow in real laser additive manufacturing condition, especially under laser powder bed fusion condition, is much more challenging, because the laser usually scans in much higher speed and the resulting melt pool is much smaller. Due to the tremendous challenge, the melt flow behavior in the entire melt pool under real laser additive manufacturing conditions has not been unveiled.

In this work, we developed an approach to trace the melt flow behavior in the whole melt pool in laser additive manufacturing by uniformly dispersing populous micro-tracers (diameter of about 5 μm) and performing in-situ high-speed high-resolution x-ray imaging. We revealed the melt flow dynamics in every location of the entire melt pool under both conduction-mode and depression-mode melting, and analyzed the driving forces of liquid flow and the physical processes in the melt pool.

2. Materials and methods

2.1 Experimental setup

In-situ high-speed high-resolution x-ray imaging was used for direct observation of the melt pool dynamics from different views during laser scanning, as schematically shown in Fig. 1(a) and Supplementary Fig. 1. The synchrotron x-ray beam (Beamline 32-ID-B, Advanced Photon Source, Argonne National Laboratory) penetrated through the metal samples and the transmitted signal was captured by a detection system [39,40,42], which recorded the videos in this work with a frame rate of 140 kHz and a spatial resolution of 1.97 μm/pixel. A continuous-wave laser beam, with a wavelength of 1070 ± 10 nm and a maximum output power of 520 W, was used to melt the powder bed. Table 1 listed the materials and detailed processing parameters in this work. Each set of parameters was repeated three times. The parameter selection for generating conduction-mode melting and depression-mode melting is based on our previous work [1]. Powders with average diameter of 35 μm were manually spread on the substrate to form a powder bed with a layer thickness of 100 ± 10 μm by using a wiper made by weighing paper. Two setups were made, one where the laser beam scans perpendicular to the x-ray beam to get the longitudinal projection of the melt pool [as shown in Fig. 1(a) and Supplementary Fig. 1(a)], and another where the laser scans parallel to the x-ray to get the transverse projection of the melt pool [as shown in the inset of Fig. 1(a) and Supplementary Fig. 1(b)]. The three-dimensional coordinate system used in this study, as indicated on the powder bed in Fig. 1(a), was defined as follows: z is the normal direction of the powder bed, y is the laser scan direction, and x is the normal direction of y-z plane, following the right-hand rule.

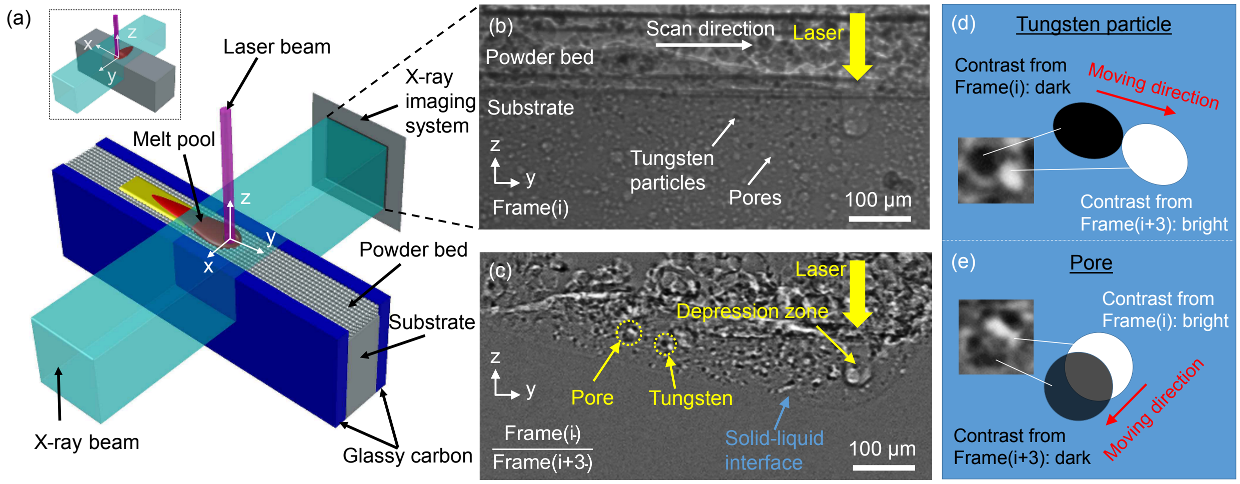

Fig. 1. Method for in-situ full-field mapping of melt flow dynamics. (a) Schematic illustration showing the in-situ x-ray imaging setup for laser powder bed fusion process. The high-speed high-resolution x-ray imaging system was used to capture the movement of tracing particles within the melt pool in the longitudinal view, as well as the transverse view (as illustrated by the simplified drawing in the inset). The x-y-z coordinate system used in this paper is indicated on the powder bed, where z is the normal direction of powder bed, y is the laser scan direction, and x is the normal direction of y-z plane, following the right-hand rule. (b) Representative x-ray image obtained at Frame(i). Uniformly dispersed populous micro-tracers (tungsten particles and pores) for melt flow tracing can be clearly identified from the x-ray image. (c) Representative x-ray image after image processing to show tracer movement and melt pool boundary. To obtain enhanced contrast, the image intensity at each pixel of Frame(i) is divided by the intensity of corresponding pixel in Frame(i+3). (d, e) Schematics showing different contrast of two types of tracers after image processing. For tungsten particle, the dark contrast comes from Frame(i) while the bright contrast comes from Frame(i+3). On the contrary, for pore, the bright contrast comes from Frame(i) and the dark contrast is from Frame(i+3). The insets in (d) and (e) are zoom-in views of the circled areas in (c).

Table 1 Materials and processing parameters

Material	Processing parameter	Melting mode
AlSi10Mg	260 W, 0.6 m/s	Conduction mode
AlSi10Mg	364 W, 0.6 m/s	Depression mode
Al-6061	520 W, 0.4 m/s	Depression mode

2.2 Materials

Two aluminum alloys, AlSi10Mg and Al-6061, were used for this study. Aluminum alloys are selected because of their high x-ray transparency. This study mainly focuses on AlSi10Mg, a widely used material for additive manufacturing. Al-6061, as a common aluminum alloy on market, was chosen to check whether the melt flow pattern observed in AlSi10Mg can also be observed in another alloy with different composition. The powder bed is composed of either AlSi10Mg or Al-6061 aluminum alloy, with the substrate material identical to the powders. To ensure better x-ray transparency, the powder bed width (along x-ray incidence) was fixed at 0.5 mm when the laser scans perpendicular to the x-ray beam (with a scan length of 2.5 mm), while 1.0 mm-thick substrates were used when the laser scan direction was parallel to the x-ray beam (with a scan length of 0.8 mm). Argon gas was used for process protection.

2.3 Flow tracing approach

Flow tracers were used to trace the melt flow during laser melting. The speed of a tracer was calculated by dividing its displacement by its travelling time. To be specific, the tracer's displacement was calculated through its 2-D coordinate change from one frame to the next in x-ray videos. The travelling time is the time interval between two frames, which was determined by the recording frame rate (140 kHz).

For the tracers to effectively indicate the movement of surrounding liquid flow, several requirements must be fulfilled: (1) The tracer must remain solid in the molten metal, meaning that tracer's melting temperature should be much higher than that of the matrix material (aluminum, in this case). (2) For the tracer to be detectable in x-ray images, the tracer must exhibit sharp contrast compared with matrix material, which means the tracer's density should be either much higher or lower than the matrix material. (3) The gravity/buoyancy of the tracer should have negligible effect on its movement. (4) The tracer must be accelerated fast enough by the surrounding liquid to avoid noticeable delay to the flow. (5) The tracer should not significantly change the viscosity of the molten liquid in the melt pool. 1 vol.% tungsten micro-particles (with an average diameter of 5 μm) in metal powders were identified as the main tracers to fulfill all the above requirements. The detailed analysis will be presented in the **Discussion** section.

The tungsten micro-particles were uniformly mixed with the feedstock aluminum powders by ball milling. Both size and amount of the tracer particles were optimized to be able to trace the melt flow in every location of the whole melt pool, yet impose minimum effect on the viscosity of the molten aluminum. Also, the small tracers used here allowed us to embed a large number of tracers under a fixed volume fraction, so that the fluid flow in every location of the melt pool could be traced accurately.

Uniformly dispersed micro-sized pores in AlSi10Mg were used as a complementary tracer, as marked in Fig. 1(b). The pores in the AlSi10Mg sample were introduced in LPBF building process. The mass density of pore is much lower than that of aluminum melt, which is used to cross-check the effect of the tracer density on melt flow tracing results. The pore movement in the main body of the melt pool was consistent with the tungsten particle movement, except for the region around depression zone (the reason for the discrepancy is explained in the **Discussion** session).

2.4 Image processing

To clearly identify the melt pool boundary and tracer movement, the raw x-ray images were processed by ImageJ to reduce noise and enhance contrast. The image intensity at each pixel of Frame(i) was divided by the intensity of corresponding pixel in Frame(i+3), so that the motionless part in the image was converted to blank background. The representative post-processed image is shown in Fig. 1(c), where the tracer movement is much clearer and the melt pool boundary is obvious. Note that the projection position of a particular tracer in Frame(i) and Frame(i+3) will both appear in a processed image, but the resulting contrasts are different for each type of tracer. For tungsten particle, the resulting contrast from Frame(i) appears to be dark in the processed image, while the resulting contrast from Frame(i+3) is bright, as illustrated in Fig. 1(d). As for the pore, the contrast from Frame(i) is bright but the contrast from Frame(i+3) is dark, as shown in Fig. 1(e).

3. Results

Different flow patterns were observed between the conduction-mode melting and depression-mode melting, due to their distinct forming mechanisms. In conduction-mode melting (also referred to as melt-in mode in welding community [50]), the material is heated up from its surface and the energy being deposited exceeds the rate at which heat is being conducted away, so that the temperature eventually reaches the melting point to form a melt pool. Under depression-mode melting, the energy from the heat source is so intense that the temperature in the material not just exceeds the melting point but reaches the boiling point. In this case, the intensive vaporization of the material applies a recoil pressure to the melt pool, thus creates a depression zone. In the welding community, the depression mode is also called "keyhole mode" when the depression zone dimension ratio (depth over half width) is larger than 1, and "transition mode" when the ratio is less than 1. Under depression mode, the heat source not just heats up the top surface of the material, but also heats up the inside of material through the depression zone. Owing to the different physics underpinning these two melting modes, the melt flow behaviors appear very differently, as detailed in the following two sections.

3.1 Melt flow pattern under conduction-mode melting

The general shape of the melt pool under conduction mode in both longitudinal view (projected in y-z plane) and transverse view (projected in x-z plane) are displayed in Figs. 2(a) and 2(c), respectively, with the melt pool boundary marked by yellow dashed line. The test was on AlSi10Mg powder bed with a laser power of 260 W and a scan speed of 0.6 m s^{-1}. The representative tracers are circled in the image, with their projectional moving directions in y-z plane indicated by arrows. The moving trend of the tracers is summarized in the corresponding schematics shown in Figs. 2(b) and 2(d). In transverse view, as displayed in Fig. 2(c), the tracers in the center plane of the melt pool move upward, while those close to the melt pool sidewalls move downward. Two vortices are thus formed with opposite circulating directions, as illustrated in Fig. 2(d). In longitudinal view [Fig. 2(a)], arrows in yellow and blue were used to distinguish the movement of tracers in the center plane and along the sidewalls. As depicted in Fig. 2(b), the flow forms a clockwise vortex ① ahead of the laser beam and a counterclockwise vortex ② behind the laser beam. The projectional flow speed (the projection of the flow velocity in the y-z plane) of three representative streams, A, B, and C will be quantified in section 3.2. The flow along the sidewalls in longitudinal view, as indicated by blue arrows in Fig. 2(b), travels from the top surface to the bottom of the melt pool, which is consistent with the observation in the transverse view [Fig. 2(c)]. A demonstration shows how the flow trend (slightly behind laser beam) shifts between the longitudinal view and the transverse view is displayed in Supplementary Movie 1. A three-dimensional reconstruction for conduction-mode melt flow is exhibited in Fig. 2(e), based on the observations above. For the clarity of illustration, the melt pool is displayed in halves, with one half (colored by cyan, transparent) showing the three-dimensional flow inside the melt pool, and the other half (colored by gray, opaque) showing the two-dimensional flow pattern only in the middle cross-section (y-z plane). The arrows in black display the flow on the top surface of melt pool, while the yellow arrows show the flow in the center plane, and the blue arrows represent the flow along the melt pool sidewalls. Different views of the three-dimensional melt flow in the whole melt pool can be found in Supplementary Movie 2.

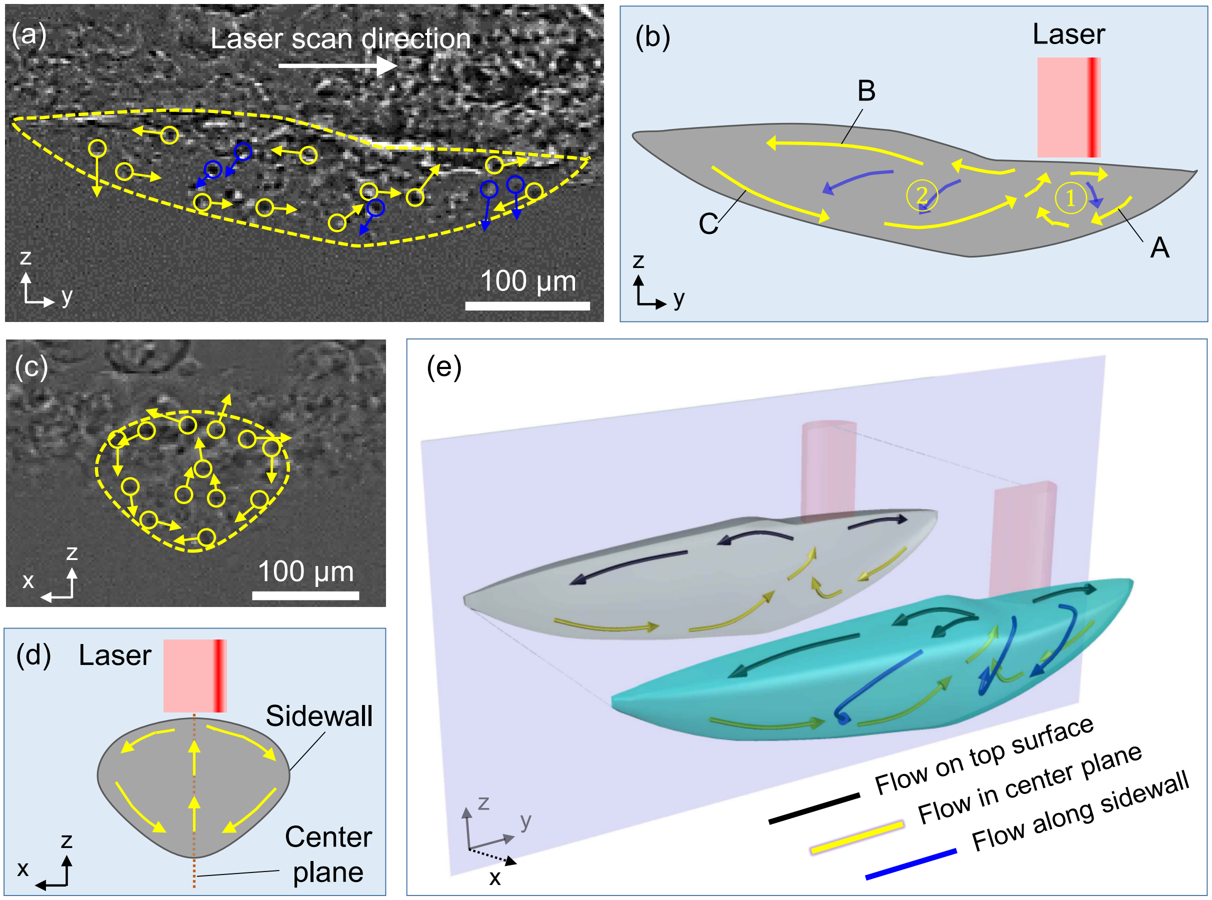

Fig. 2. Melt flow behavior under conduction mode. (a) X-ray image showing the instantaneous liquid flow direction in y-z projection plane (longitudinal view). (b) Schematic summarizing the melt flow pattern in y-z projection plane. (c) X-ray image showing the instantaneous liquid flow pattern in x-z plane (transverse view). (d) Schematic summarizing the melt flow pattern in x-z projection plane. (e) Reconstruction of three-dimensional melt flow pattern. All the tests were carried out on AlSi10Mg powder bed with a laser power of 260 W and a laser scan speed of 0.6 m s^{-1}. The laser D4σ diameter is around 80 μm.

3.2 Melt flow pattern under depression-mode melting

With the formation of depression, the laser beam directly interacts with the interior of melt pool, which promotes the energy absorption that leads to much larger melt pool with more complex flow pattern as compared with that under conduction mode. To facilitate the description, the melt pool is divided into three regions [i.e., tail, body, and head, as shown in Figs. 3(a)-3(c), respectively] along the laser scan direction. The arrows in yellow and blue, similar to conduction mode, were used to distinguish the tracer motions in the center plane and along the sidewalls. In the transverse view of melt pool, to differentiate the flow patterns around the depression from those in the body of melt pool (behind depression), the flow behavior was recorded during laser scanning [Fig. 3(e)] and 50 μs after the laser was off [before the contraction of the melt pool boundary, as displayed in Fig. 3(g)], respectively. Note that t_o is the moment when the laser was turned off.

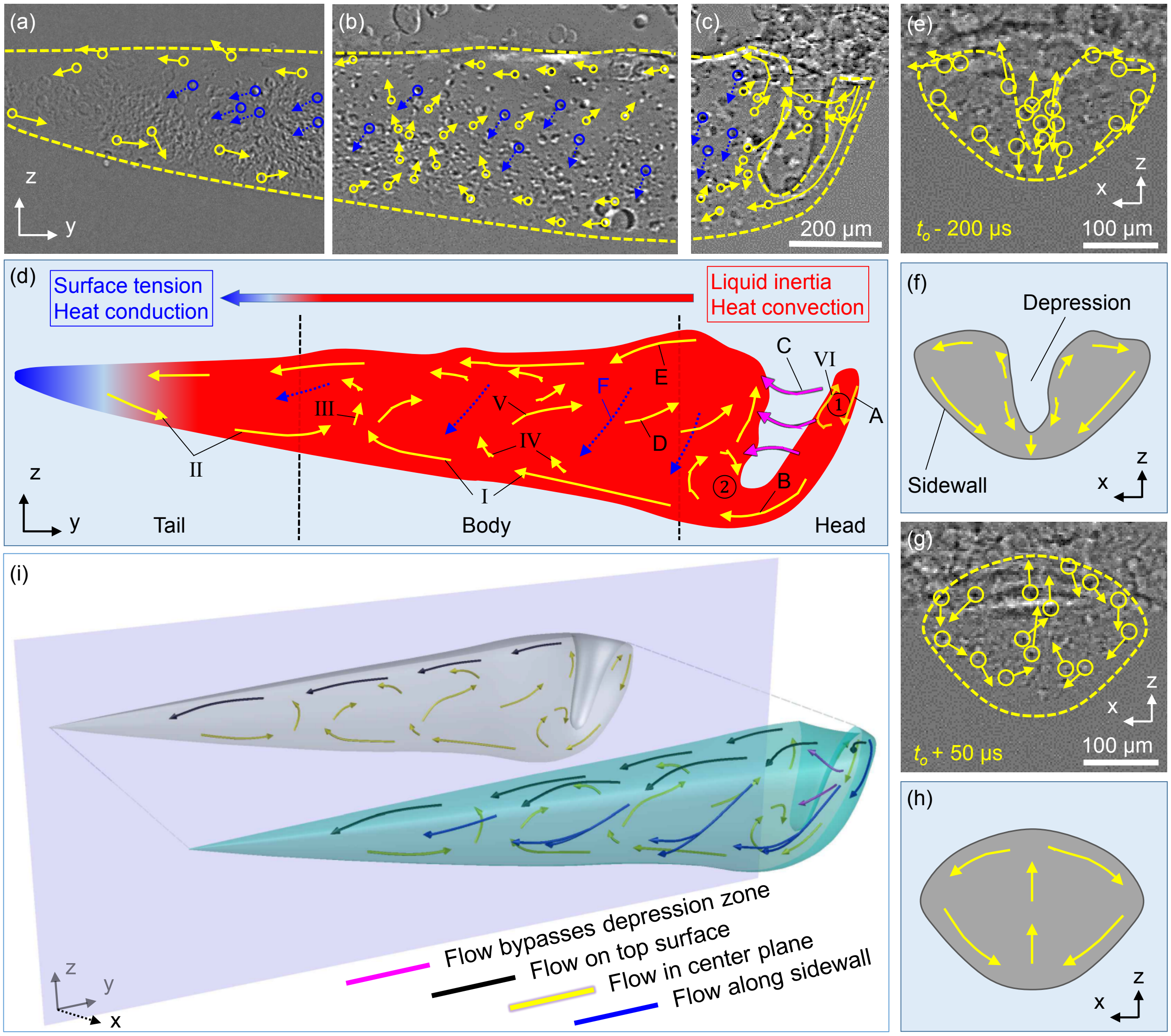

Fig. 3. Melt flow behavior under depression mode. (a)-(c) X-ray images showing the instantaneous liquid flow direction in y-z projection plane. (d) Schematic summarizing the flow pattern in y-z projection plane. (e), (g) X-ray images displaying the flow pattern around depression zone (e) and behind depression zone (g) in x-z projection plane. (f), (h) Schematics summarizing the flow pattern around depression zone (f) and behind depression zone (h) in x-z projection plane. (i) Reconstruction of three-dimensional melt flow pattern under depression mode. The tests were carried out on AlSi10Mg powder bed with 364 W laser power and 0.6 m s^{-1} scan speed. t_o is the moment when the laser was turned off.

The trend of tracer motions in Figs. 3(a)-3(c) is summarized and combined together in the schematic Fig. 3(d), while the tracer movement in Fig. 3(e), 3(g) are depicted in schematic Figs. 3(f), 3(h). Six types of flow that marked by A-F in Fig. 3(d) will be quantified in section 3.3.

In the center plane, as shown in Fig. 3(d), the flow around the depression moves upward near the depression outlet, while moves downward near the bottom of depression, which is consistent with the flow pattern around the depression in transverse view [Fig. 3(f)]. The flow bypasses the depression travels in the opposite direction to the laser scan direction, as illustrated by flow C in Fig. 3(d). The flow near the melt pool surface moves backward, from depression outlet to the tail of melt pool. The flow at the bottom of melt pool (flow I) also has a main trend of moving backward, except a short forward flow (flow II) was observed at the rear bottom of melt pool. Flow I and II collide to form a merged flow (flow III) which moves upwards and splits into flows of opposite directions. In the area between the top and bottom backward flow, as pointed out by flow D in Fig. 3(d), the general flow movement in the center plane have a tendency of going forward and upward, which is consistent with the observation of flow pattern in transverse view [Fig. 3(h)]. The flow along the sidewalls of the melt pool moves downward, as displayed by the blue arrows in Fig. 3(d), which is in accordance with the transverse-view observations in Figs. 3(f), 3(h). Two movies (Supplementary Movies 3, 4) were made to demonstrate the flow pattern transition (around depression and behind depression) between the longitudinal view and transverse view. A three-dimensional reconstruction of depression-mode melt flow is shown in Fig. 3(i). The arrows in magenta show the flow bypasses the depression, while the black arrows display the flow on the top surface of melt pool, the yellow arrows show the flow in the center plane, and the blue arrows represent the flow along the melt pool sidewalls. The different views of the three-dimensional melt flow in the whole melt pool is shown in Supplementary Movie 5.

To confirm that the above melt flow pattern is not limited to an alloy with a specific composition, tests on Al-6061 were carried out. Very similar melt flow pattern in depression-mode melting was observed, as displayed in Fig. 4.

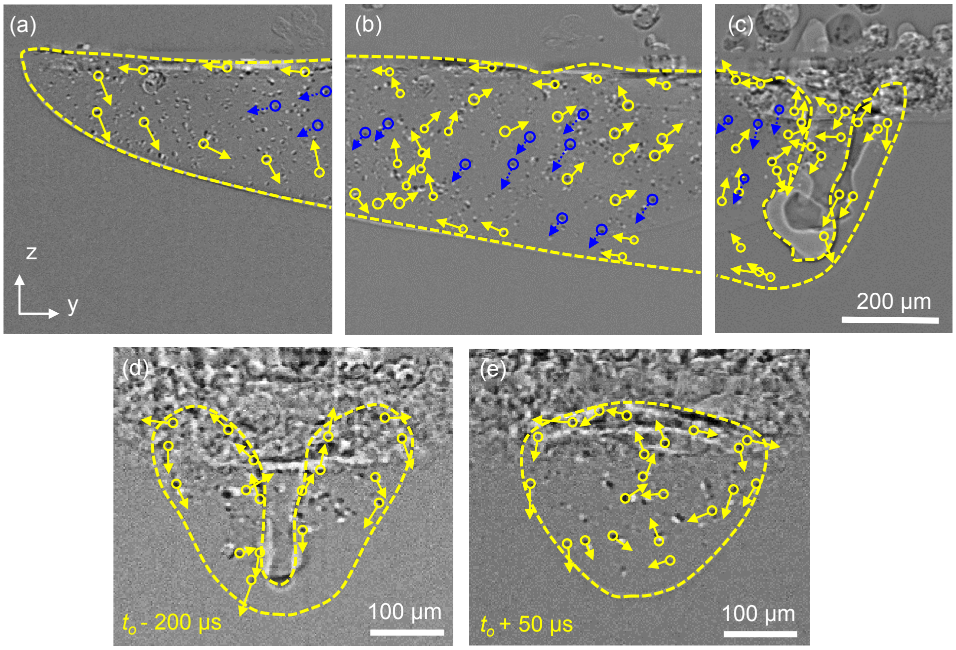

Fig. 4. Melt flow pattern in Al-6061. (a-c) X-ray images showing the instantaneous liquid flow direction in y-z projection plane. (d, e) X-ray images displaying the flow pattern around depression zone (d) and behind depression zone (e) in x-z projection plane. The tests were carried out on Al-6061 powder bed with 520 W laser power and 0.4 m/s scan speed.

3.3 Quantification of flow speed

The projectional speed of melt flow A, B, C [as marked in Fig. 2(b)] under conduction mode and flow A, B, C, D, E, F [as marked in Fig. 3(d)] under depression mode were measured and shown in Figs. 5(a), 5(b), respectively. The flow direction and location were detailed in Table 2. Note that the flow E, D, F in depression mode were only quantified within a 300 µm region after the depression (as we will show later in Fig. 6 that the flow speed attenuates fast at the tail of melt pool). Since the tracers at different locations (e.g., in the center vs. near the edge) of a particular flow stream may have different speeds, the average speeds of each type of flow and the standard deviations are calculated and displayed by blue bars. In addition, the maximum speeds of each type of flow are shown in the histograms by red bars as a useful measure, given that the three-dimensional motion of the tracers may have components perpendicular to view plane. Under both conduction mode and depression mode, flow A (downward flow along the front melt pool boundary) has the highest speed, with maximum speed values of 2.83 m s^{-1} for conduction mode and 3.68 m s^{-1} for depression mode.

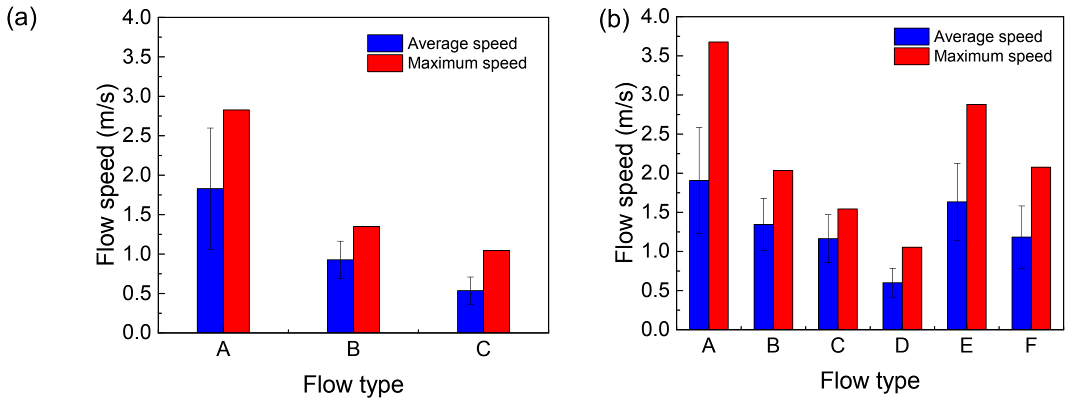

Fig. 5. Quantification of flow speed under conduction mode (a) and depression mode (b) as a function of flow type. The flow types A, B, and C under conduction mode were marked in Fig. 2(b). The flow types A-F under depression mode were indicated in Fig. 3(d).

Table 2. Types of flow and their locations

Melting mode	Flow type	Flow direction	Flow location
Conduction	A	Backward	Along the front melt pool bottom
	B	Backward	Along the melt pool surface
	C	Forward	Along the rear melt pool bottom
Depression	A	Downward	Along the front depression wall
	B	Downward & backward	Along the depression bottom
	C	Backward	Around the depression zone
	D	Upward & forward	Toward the depression outlet
	E	Backward	Along the surface of melt pool
	F	Downward & backward	Along the sidewall of melt pool

The above measurements provide speed information of each type of flow in localized regions. Further quantification was carried out to analyze the general trend of the flow speed as a function of location across the melt pool. Quantification was first carried out on AlSi10Mg [Figs. 6(a), 6(b)] and then on Al-6061 [Figs. 6(c), 6(d)]. From the middle of rear depression wall [as marked by red dot in Fig. 6(a)], the melt pool behind the reference position was divided into 12 sections with 100 μm segment width. The projectional speed of the tracers in each section (Y_i) were measured and plotted in Fig. 6(b). Both the average speed and maximum speed exhibit a general decreasing trend as a function of the distance from depression. In the first section Y_1, the average speed is 0.52 m/s and the maximum speed is 1.25 m/s. In the last section Y_{12}, the average speed is 0.08 m/s and the maximum speed is 0.15 m/s, which are both an order of magnitude lower than those in section Y_1. The quantification stopped at Y_{12} because the flow speed is so low that approaches the measurement precision (0.025 m/s). The same quantification strategy was applied to Al-6061 melt pool, as shown in Fig. 6(c). Similar decreasing trend of the speeds were observed, as shown in Fig. 6(d).

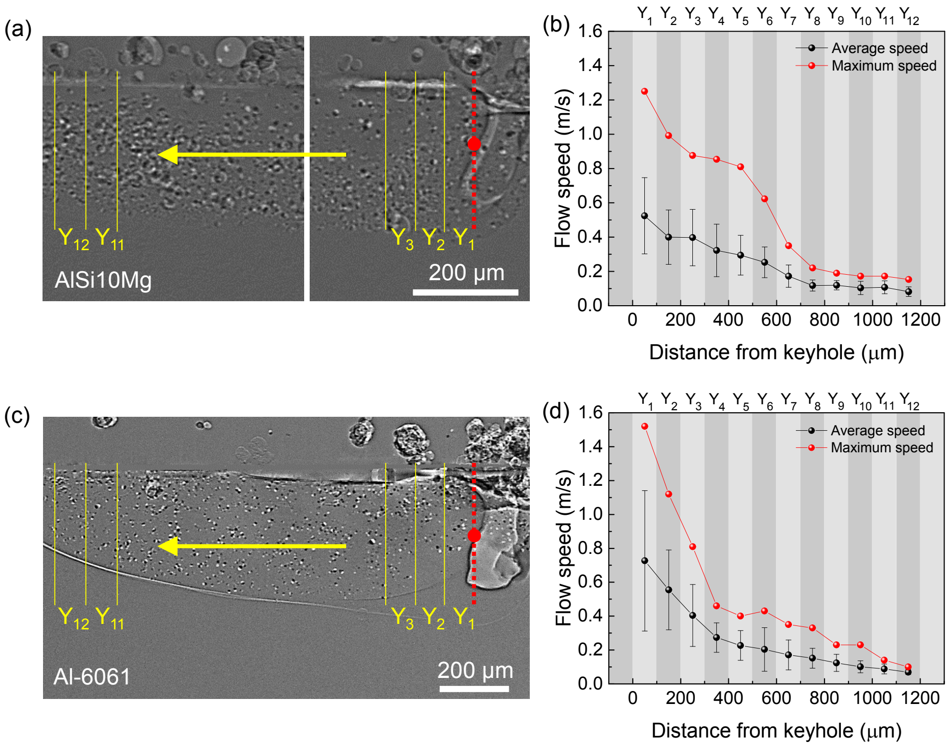

Fig. 6. Quantification of flow speed along melt pool. (a) X-ray image illustrating the quantification method of flow speed as a function of location behind depression zone. Note that two images were jointed together here to display the full quantification length. The test was carried out on AlSi10Mg. The middle of rear depression wall was set as the reference point. The projectional flow speeds in the rest part of melt pool were averaged in consecutive sections with an increment of 100 μm. (b) The measured average and maximum projectional flow speed as a function of location. (c, d) Quantification of flow speed in Al-6061 melt pool.

Due to the highly dynamic nature of the depression zone, the general flow speed ahead of rear depression wall was not quantified in the above analysis. Instead, a particular tracer that moved all the way down in the thin liquid film ahead of depression zone was tracked to reveal the flow behavior at the depression area, as displayed in Fig. 7(a). This tracer is special, because its trajectory is rarely seen during the experiments. As illustrated in Fig. 3(d), if a tracer wants to move all the way down along the liquid film ahead of the depression, it needs to experience flow A and then flow B. However, due to the coaction of the vortex ① and the strong side flow C, most tracers entering the depression front will be dragged to other directions, and only the ones happen to be at the exact center of the depression front film could continue to flow downward, as illustrated by the inset in Fig. 7(b). Therefore, the tracer that was tracked in Fig. 7(a) must have moved in the y-z plane with minimum speed component in x-direction. This tracer's speed can then reflect the real speed of downward flow ahead of the depression zone. Fig. 7(b) indicates that its speed dropped dramatically in the liquid film ahead of depression zone, decreasing by around 90% from 4.5 m s^{-1} (0 μs) to 0.45 m s^{-1} (64 μs), and then became relatively stable when it entered the main body of the melt pool.

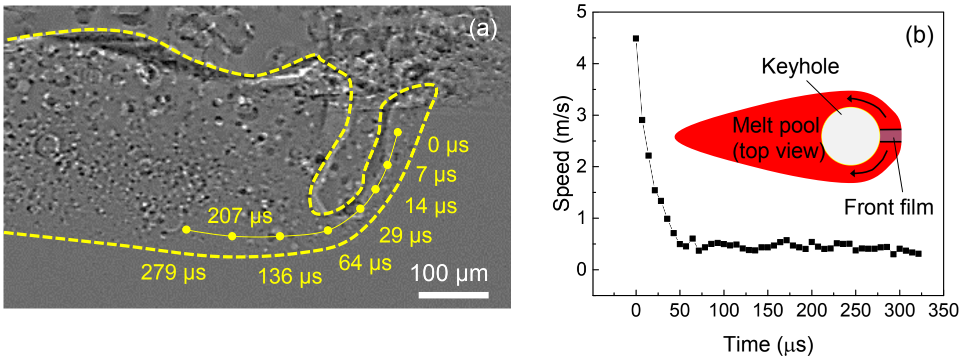

Fig. 7. Quantification of flow speed along front depression wall. (a) X-ray image displaying the trajectory of a tracing particle travelling along front depression wall. The test was done on AlSi10Mg powder bed. Note that the yellow dot size in the image does not represent the real size of the tracing particle. (b) The speed of tracing particle as a function of time.

4. Discussion

4.1 Validity of flow tracing by tracer particles

To examine the effect of gravity/buoyancy on tracer movements, the settling velocity (v_p) of tungsten particle in liquid AlSi10Mg was calculated to be $v_p = 1.3\times10^{-4}$ m s^{-1} by the Stokes's law [51,52] (the detailed calculation is in Supplementary Note 1). The settling velocity is the terminal velocity for a free-fall particle in the liquid that only has gravity, buoyancy, and friction force on it. The calculated settling velocity is at least two orders of magnitude lower than the flow speeds measured in this work, meaning that the detected tracer speed must under strong influence from surrounding flow, otherwise their velocity will be closer to the settling velocity. To further confirm that the high-density tungsten micro-tracer does not influence the tracing results in our work, gas pores (almost zero density) are used as complementary tracers. Our results show that the pore movement in the main body of the melt pool is consistent with the tungsten particle movement. However, pores cannot be used as melt flow tracers in the depression region. The mechanism for this discrepancy was recently reported in [8].

To examine whether the tracer can be accelerated fast enough by the surrounding liquid, the tracer in Fig. 7(a) was investigated as an example because it entered into the front depression wall, where the flow moves the fastest (> 4.5 m/s) among the melt pool. Assuming the particle was accelerated to the maximum speed within one frame (~ 7 μs), the maximum acceleration of the tracer can be calculated to be 6.4×10^{5} m s^{-2}, which is equivalent to a force of 0.81 μN by Newton's second law. However, the maximum drag force provided by the molten aluminum flow, by the Schiller-Naumann drag law [34], is calculated to be 4.2 μN (see Supplementary Note 2 for details), which can provide the particle with an acceleration of 5 times as much as it really needs. It was calculated that the tungsten particle can be accelerated to over 50% of the surrounding flow speed within 1.4 μs (see Supplementary Note 2 for details). Furthermore, within one frame (~7 μs), the tracer speed can be accelerated to over 85% of the flow speed. Since the motion delay between the micro-tracer particle (5 μm in size) and the surrounding flow is negligible, the tracers' movement can indeed reflect the liquid flow in the present experimental conditions.

To examine the effect of tracers on the viscosity of the liquid, it is calculated that the liquid with 1 vol.% tracer particles has a viscosity of 2.6% higher than the one without particles (see Supplementary Note 3 for details). In practice, the viscosity will increase less than 2.6% because the tracer concentration in the liquid will be lower than 1 vol%, considering that the substrate does not contain tracer particles before melting. Besides, none of the experiments exhibited significant local particle density variation, e.g. clusters or aggregations, in the melt pool. Thus, mixing 1 vol.% tungsten particles into feedstock powder will not significantly alter the viscosity of the melt and the flow pattern in the melt pool.

4.2 Analysis of driving forces for liquid flow in melt pool

The complex flow patterns revealed in this work have not been completely replicated by the models and simulations published so far. To understand the physics underlying melt flow pattern, the driving forces in the melt pool that account for the various flow patterns observed in different regions are analyzed below.

There are five major driving forces in the melt pool. Marangoni force drives the flow from high temperature region to low temperature region for a material with a negative temperature coefficient of surface tension (from low surface tension region to high surface tension region, most metals and alloys exhibit negative temperature coefficient of surface tension) [4,21,38,53,54]. Vaporization induced recoil pressure exerts an inward pressure normal to the vaporization surface [6,30]. High-speed vapor plume (can reach 10^2-10^3 m s^{-1} [55]) can induce shear force through friction at the liquid-gas interface [33,53]. Hydraulic pressure can exchange energy by either pressure (hydrostatic pressure) or by momentum (hydrodynamic pressure) [5]. Buoyance force drives liquid along density gradient [5,18,26]. The details about each type of driving forces can be found in Supplementary Notes 4-7.

In conduction-mode melt pool, the dominating driving force is Marangoni force, which drives the melt flow from hotter region to cooler region (the materials we studied have negative temperature coefficient of surface tension), i.e., from laser heating spot to melt pool rim. Therefore, in longitudinal view [Fig. 2(b)] the surface flow ahead of laser beam moves forward, while the one behind laser beam moves backward. When the flows reach each rim of melt pool, they will flow downward and return to the laser heating spot under the effect of hydraulic pressure. Thus, two close loops are formed: a clockwise loop ahead of laser beam and a counterclockwise loop behind the laser beam. Driven also by Marangoni force, the flows in transverse view [Fig. 2(d)] form another two close loops (consistent with recent research [38]), following a similar mechanism as in longitudinal view.

The flow pattern in depression-mode melt pool is rather complex, due to the intense vaporization induced depression zone. The vaporization-related forces, i.e., the recoil pressure and the vapor plume friction, dominate the flow pattern around the depression [the “Head” region in Fig. 3(d)]. The flow around the upper part of depression moves upward under Marangoni force [28] and the vapor plume friction [14,30], while the flow close to the bottom of depression moves downward due to the recoil pressure, as can be seen in both longitudinal view [Fig. 3(d), flow B] and transverse view [Fig. 3(f)]. The flow bypasses the depression zone is mainly driven by hydraulic pressure gradient, as a high-hydraulic pressure region is formed in the liquid film ahead of depression zone while the front depression wall keeps “pressing” the front liquid during its travelling. Note that the upward flow VI in vortex ① may temporarily disappear or enhance, which is hypothesized to be depending on the competition between the downward recoil pressure and the upward vapor plume friction on the front depression wall [30,33,53]. With the proceeding of depression zone, a low hydraulic-pressure region forms behind the bottom of depression [25], which drains the surrounding liquid into this region and thus induces the vortex ②. For the “Body” part of melt pool, as shown in Fig. 3(d), the surface flow moves backward from high temperature region to low temperature region (Marangoni force), similar to the condition of conduction-mode melting. The flow at the bottom (flow I) inherits the momentum from flow B and thus moves backward. Being freshly heated up at the depression, the flow I carries higher temperature liquid (with lower density) than those in the upper level within the melt pool. Therefore, the molten metal in flow I floats up (flow IV) under the buoyancy force during the backward transportation. The flow in the middle level of melt pool (flow D and V), aside from the upward movement, has a main tendency of moving forward, attracted by the low hydraulic pressure region around depression zone induced by the high-speed flows under Bernoulli's effect. At the "Tail" region of melt pool, the backward flow on the surface is driven by Marangoni force, while the flow II is generated when the surface flow bounces back at the melt pool rim. During the colliding of flow I and II, the momentum transfers from flow I and II to their merged flow—flow III.

4.3 Analysis of physical processes in the melt pool

Based on the quantitative analysis provided above, physical processes associated with kinetic energy damping and heat transfer are analyzed at different locations in the melt pool.

4.3.1 Liquid momentum versus surface tension

The extent of damping the flow, especially on the surface (mainly dominated by Marangoni convection), can be expressed by Weber number (We) as

$$We = \frac{\rho v^2 L}{\sigma} \tag{1}$$

where ρ is the liquid density, v is the flow speed, L is the characteristic length, and σ is the surface tension [23]. The Weber number is calculated to be $We = 1.78$ near the depression zone and $We = 0.007$ near the melt pool tail. It means that the inertia of the liquid overcomes the surface tension near depression region (where Marangoni convection/recoil pressure is strong), then becomes much less important when approaching the tail of the melt pool, as schematically shown in Fig. 3(d). Consequently, the melt pool surface at the head of melt pool is more rippled, caused by the momentum of upward liquid along the rear depression wall, while the surface at the tail of melt pool is rather flat and smooth because the surface tension will damp out the surface wave.

4.3.2 Heat conduction versus heat convection

To improve the computing efficiency and speed, some simplified modelling work (based on heat transfer theories) on laser processing choose to only consider the effect of heat conduction while neglect the effect of heat convection [13,56]. Here we show that the heat convection should not be neglected, as it is significant near the head of melt pool. With the measured flow speed, the relative effect of heat convection over heat conduction can be evaluated by the Péclet number (Pe), which is the product of Reynolds number (Re_L) and Prandtl number (Pr) as

$$Pe = Re_L \cdot Pr = \frac{\rho v L}{\mu} \cdot \frac{c_p \mu}{k} = \frac{L v}{\alpha} \tag{2}$$

where L is the characteristic length, v is the local flow speed, and α is the thermal diffusivity. Taking the test in Fig. 6(a) as an example, $v = 1.25$ m s^{-1}, $\alpha = 6.6\times10^{-5}$ m^2 s^{-1} in section Y_1 near the depression zone; and $v = 0.08$ m s^{-1}, $\alpha = 3.54\times10^{-5}$ m^2 s^{-1} in section Y_{12} near the tail of melt pool. The characteristic length (L) is chosen as the hydraulic diameter (D_h) of the melt pool. In section Y_1, $L = D_h = 539$ µm; in section Y_{12}, $L = D_h = 427$ µm. (Method to calculate the hydraulic diameter is detailed in Supplementary Note 8.) The Péclet number is calculated to be $Pe_{(head)} = 10.2$ at the head of melt pool and $Pe_{(tail)} = 0.9$ at the tail. When Pe $\geq$ 10, qualitatively, heat convection is considered to make a greater contribution to the thermal energy transportation [12]. The results indicate a strong heat convection could occur at the head of melt pool while heat conduction is dominating at the tail of melt pool. The prevailing physical processes along the melt pool were indicated in Fig. 3(d).

4. Conclusions

In the present work, for the first time, we revealed and quantified the melt flow dynamics in every location of the entire melt pool in laser metal additive manufacturing process under both conduction-mode and depression-mode melting. The major conclusions are detailed below:

(1) We developed a full-field melt flow mapping method to reveal the detailed melt flow dynamics under laser metal additive manufacturing conditions by tracing uniformly dispersed populous micro-tracers through in-situ high-speed high-resolution x-ray imaging.

(2) The melt flow behaviors were revealed in every location of the whole melt pool under both conduction-mode and depression-mode melting in laser additive manufacturing process. The conduction-mode melt pool possesses a simple flow pattern that is mainly driven by the Marangoni effect, while the flow pattern in depression-mode melt pool is rather complex, under the coaction of multiple driving forces. The flow pattern and flow speed are location dependent. The detailed (projectional) flow speeds in different regions of the melt pool under both conduction-mode and depression-mode melting were quantified in terms of average speed and maximum speed. Decreasing of the flow speed from the depression zone to the melt pool tail was observed and statistically analyzed.

(3) The driving forces for different types of melt flow were analyzed. Marangoni effect accounts for the flow movement from high-temperature region to low-temperature region (for a material with a negative temperature coefficient of surface tension) on the surface of the melt pool. Vaporization dominates the fluid flow along depression-zone walls. Hydraulic pressure

drives fluid flow from high-pressure region to low-pressure region. Buoyance force accounts for liquid convection from low-density region to high-density region.

(4) The prevailing physical processes concerning kinetic energy damping and heat transfer at the head of melt pool were experimentally identified to be liquid inertia and heat convection, respectively; while at the tail of melt pool, correspondingly, the physical processes were determined to be surface tension and heat conduction.

The full-field melt flow mapping approach reported here opens the way to study the melt flow dynamics under real additive manufacturing conditions. Our findings reported here are critical for not only understanding the laser additive manufacturing process and other laser processes, but also for developing reliable high-fidelity computational models.

Acknowledgements

The authors would like to thank Alex Deriy at the APS for his help on the beamline experiments. Q.G., M.Q., L.X., S.M.H.H., L.I.E., and L.C. acknowledge the financial support by National Science Foundation (Award No. 1762477). C.Z., N.D.P., K.F, and T.S. thank the Laboratory Directed Research and Development (LDRD) funding from Argonne National Laboratory, provided by the Director, Office of Science, of the U.S. Department of Energy under Contract No. DE-AC02-06CH11357. This research used resources of the Advanced Photon Source, a U.S. Department of Energy (DOE) Office of Science User Facility operated for the DOE Office of Science by Argonne National Laboratory under Contract No. DE-AC02-06CH11357.

References

[1] Q. Guo, C. Zhao, M. Qu, L. Xiong, L.I. Escano, S.M.H. Hojjatzadeh, N.D. Parab, K. Fezzaa, W. Everhart, T. Sun, L. Chen, In-situ characterization and quantification of melt

pool variation under constant input energy density in laser powder bed fusion additive manufacturing process, Addit. Manuf. 28 (2019) 600–609. doi:10.1016/j.addma.2019.04.021.

[2] Y. Kawahito, M. Mizutani, S. Katayama, Elucidation of high-power fibre laser welding phenomena of stainless steel and effect of factors on weld geometry, J. Phys. D. Appl. Phys. 40 (2007) 5854–5859. doi:10.1088/0022-3727/40/19/009.

[3] S. Katayama, Y. Kawahito, M. Mizutani, Elucidation of laser welding phenomena and factors affecting weld penetration and welding defects, Phys. Procedia. 5 (2010) 9–17. doi:10.1016/j.phpro.2010.08.024.

[4] F. Tenner, B. Berg, C. Brock, F. Klämpfl, M. Schmidt, Experimental approach for quantification of fluid dynamics in laser metal welding, J. Laser Appl. 27 (2015) S29003. doi:10.2351/1.4906302.

[5] B. Chang, C. Allen, J. Blackburn, P. Hilton, D. Du, Fluid flow characteristics and porosity behavior in full penetration laser welding of a titanium alloy, Metall. Mater. Trans. B. 46 (2015) 906–918. doi:10.1007/s11663-014-0242-5.

[6] I. Eriksson, J. Powell, A.F.H. Kaplan, Melt behavior on the keyhole front during high speed laser welding, Opt. Lasers Eng. 51 (2013) 735–740. doi:10.1016/j.optlaseng.2013.01.008.

[7] S. Shrestha, S. Rauniyar, K. Chou, Thermo-fluid modeling of selective laser melting: single-track formation incorporating metallic powder, J. Mater. Eng. Perform. 28 (2019) 611–619. doi:10.1007/s11665-018-3574-5.

[8] S.M.H. Hojjatzadeh, N.D. Parab, W. Yan, Q. Guo, L. Xiong, C. Zhao, M. Qu, L.I. Escano, X. Xiao, K. Fezzaa, W. Everhart, T. Sun, L. Chen, Pore elimination mechanisms during 3D printing of metals, Nat. Commun. 10 (2019) 3088. doi:10.1038/s41467-019-10973-9.

[9] K.N. Kowal, S.H. Davis, Strong shear-flow modulation of instabilities in rapid directional solidification, Acta Mater. 164 (2019) 464–472. doi:10.1016/j.actamat.2018.10.054.

[10] Y. Zhao, Y. Koizumi, K. Aoyagi, D. Wei, K. Yamanaka, A. Chiba, Molten pool behavior and effect of fluid flow on solidification conditions in selective electron beam melting (SEBM) of a biomedical Co-Cr-Mo alloy, Addit. Manuf. 26 (2019) 202–214. doi:10.1016/j.addma.2018.12.002.

[11] T. DebRoy, H.L. Wei, J.S. Zuback, T. Mukherjee, J.W. Elmer, J.O. Milewski, A.M. Beese, A. Wilson-Heid, A. De, W. Zhang, Additive manufacturing of metallic components – Process, structure and properties, Prog. Mater. Sci. 92 (2018) 112–224. doi:10.1016/j.pmatsci.2017.10.001.

[12] Y. Kawahito, Y. Uemura, Y. Doi, M. Mizutani, K. Nishimoto, H. Kawakami, M. Tanaka, H. Fujii, K. Nakata, S. Katayama, Elucidation of the effect of welding speed on melt flows in high-brightness and high-power laser welding of stainless steel on basis of three-dimensional X-ray transmission in situ observation, Weld. Int. 31 (2017) 206–213. doi:10.1080/09507116.2016.1223204.

[13] S.A. Khairallah, A.T. Anderson, A. Rubenchik, W.E. King, Laser powder-bed fusion additive manufacturing: Physics of complex melt flow and formation mechanisms of pores, spatter, and denudation zones, Acta Mater. 108 (2016) 36–45. doi:10.1016/j.actamat.2016.02.014.

[14] Y. Kawahito, K. Nakada, Y. Uemura, M. Mizutani, K. Nishimoto, H. Kawakami, S. Katayama, Relationship between melt flows based on three-dimensional X-ray transmission in situ observation and spatter reduction by angle of incidence and defocussing distance in high-power laser welding of stainless steel, Weld. Int. 32 (2018) 485–496. doi:10.1080/01431161.2017.1346887.

[15] P. Yuan, D. Gu, Molten pool behaviour and its physical mechanism during selective laser melting of TiC/AlSi10Mg nanocomposites: simulation and experiments, J. Phys. D. Appl. Phys. 48 (2015) 035303. doi:10.1088/0022-3727/48/3/035303.

[16] A. Matsunawa, J.-D. Kim, N. Seto, M. Mizutani, S. Katayama, Dynamics of keyhole and molten pool in laser welding, J. Laser Appl. 10 (1998) 247–254. doi:10.2351/1.521858.

[17] M. Xia, D. Gu, G. Yu, D. Dai, H. Chen, Q. Shi, Selective laser melting 3D printing of Ni-based superalloy: understanding thermodynamic mechanisms, Sci. Bull. 61 (2016) 1013–1022. doi:10.1007/s11434-016-1098-7.

[18] M. Sohail, S.-W. Han, S.-J. Na, A. Gumenyuk, M. Rethmeier, Characteristics of weld pool behavior in laser welding with various power inputs, Weld. World. 58 (2014) 269–277. doi:10.1007/s40194-014-0112-4.

[19] Z. Gan, G. Yu, X. He, S. Li, Surface-active element transport and its effect on liquid metal flow in laser-assisted additive manufacturing, Int. Commun. Heat Mass Transf. 86 (2017) 206–214. doi:10.1016/j.icheatmasstransfer.2017.06.007.

[20] S.K. Rauniyar, K. Chou, Melt pool analysis and mesoscale simulation of laser powder bed fusion process (L-PBF) with Ti-6Al-4V powder particles, JOM. 71 (2019) 938–945. doi:10.1007/s11837-018-3208-2.

[21] K. Abderrazak, S. Bannour, H. Mhiri, G. Lepalec, M. Autric, Numerical and experimental study of molten pool formation during continuous laser welding of AZ91 magnesium alloy, Comput. Mater. Sci. 44 (2009) 858–866. doi:10.1016/j.commatsci.2008.06.002.

[22] M. Courtois, M. Carin, P. Le Masson, S. Gaied, A two-dimensional axially-symmetric model of keyhole and melt pool dynamics during spot laser welding, Rev. Métallurgie. 110 (2013) 165–173. doi:10.1051/metal/2013060.

[23] M. Bachmann, V. Avilov, A. Gumenyuk, M. Rethmeier, About the influence of a steady magnetic field on weld pool dynamics in partial penetration high power laser beam welding of thick aluminium parts, Int. J. Heat Mass Transf. 60 (2013) 309–321. doi:10.1016/j.ijheatmasstransfer.2013.01.015.

[24] L. Zhang, J. Zhang, G. Zhang, W. Bo, S. Gong, An investigation on the effects of side assisting gas flow and metallic vapour jet on the stability of keyhole and molten pool during laser full-penetration welding, J. Phys. D. Appl. Phys. 44 (2011) 135201. doi:10.1088/0022-3727/44/13/135201.

[25] T. Zhang, H. Li, S. Liu, S. Shen, H. Xie, W. Shi, G. Zhang, B. Shen, L. Chen, B. Xiao, M. Wei, Evolution of molten pool during selective laser melting of Ti–6Al–4V, J. Phys. D. Appl. Phys. 52 (2019) 055302. doi:10.1088/1361-6463/aaee04.

[26] J. Peng, L. Li, S. Lin, F. Zhang, Q. Pan, S. Katayama, High-speed x-ray transmission and numerical study of melt flows inside the molten pool during laser welding of aluminum alloy, Math. Probl. Eng. 2016 (2016) 1–13. doi:10.1155/2016/1409872.

[27] N. Kouraytem, X. Li, R. Cunningham, C. Zhao, N. Parab, T. Sun, A.D. Rollett, A.D. Spear, W. Tan, Effect of laser-matter interaction on molten pool flow and keyhole

dynamics, Phys. Rev. Appl. 11 (2019) 064054. doi:10.1103/PhysRevApplied.11.064054.

[28] P. Jin, Z. Wenjie, W. Xingxing, G. Guoquan, Z. Furong, Numerical simulation of effect of filler wire melting and filling mode on molten pool in laser welding, Infrared Laser Eng. 47 (2018) 306005. doi:10.3788/IRLA201847.0306005.

[29] M. Xia, D. Gu, G. Yu, D. Dai, H. Chen, Q. Shi, Porosity evolution and its thermodynamic mechanism of randomly packed powder-bed during selective laser melting of Inconel 718 alloy, Int. J. Mach. Tools Manuf. 116 (2017) 96–106. doi:10.1016/j.ijmachtools.2017.01.005.

[30] H. Nakamura, Y. Kawahito, K. Nishimoto, S. Katayama, Elucidation of melt flows and spatter formation mechanisms during high power laser welding of pure titanium, J. Laser Appl. 27 (2015) 032012. doi:10.2351/1.4922383.

[31] M. Courtois, M. Carin, P. Le Masson, S. Gaied, M. Balabane, Guidelines in the experimental validation of a 3D heat and fluid flow model of keyhole laser welding, J. Phys. D. Appl. Phys. 49 (2016) 155503. doi:10.1088/0022-3727/49/15/155503.

[32] M. Schaefer, S. Kessler, F. Fetzer, T. Graf, Influence of the focal position on the melt flow during laser welding of steel, J. Laser Appl. 29 (2017) 012010. doi:10.2351/1.4972098.

[33] A. Matsunawa, N. Seto, M. Mizutani, S. Katayama, Liquid motion in keyhole laser welding, in: Int. Congr. Appl. Lasers Electro-Optics, Laser Institute of America, 1998: pp. G151–G160. doi:10.2351/1.5059193.

[34] F. Wirth, S. Arpagaus, K. Wegener, Analysis of melt pool dynamics in laser cladding and direct metal deposition by automated high-speed camera image evaluation, Addit. Manuf.

21 (2018) 369–382. doi:10.1016/j.addma.2018.03.025.

[35] H. Wang, M. Nakanishi, Y. Kawahito, Dynamic balance of heat and mass in high power density laser welding, Opt Express. 26 (2018) 6392–6399. doi:10.1364/OE.26.006392.

[36] Y. Naito, M. Mizutani, S. Katayama, Effect of oxygen in ambient atmosphere on penetration characteristics in single yttrium–aluminum–garnet laser and hybrid welding, J. Laser Appl. 18 (2006) 21–27. doi:10.2351/1.2164484.

[37] S. Katayama, Y. Kobayashi, M. Mizutani, A. Matsunawa, Effect of vacuum on penetration and defects in laser welding, J. Laser Appl. 13 (2001) 187–192. doi:10.2351/1.1404413.

[38] L. Aucott, H. Dong, W. Mirihanage, R. Atwood, A. Kidess, S. Gao, S. Wen, J. Marsden, S. Feng, M. Tong, T. Connolley, M. Drakopoulos, C.R. Kleijn, I.M. Richardson, D.J. Browne, R.H. Mathiesen, H. V Atkinson, Revealing internal flow behaviour in arc welding and additive manufacturing of metals, Nat. Commun. 9 (2018) 5414. doi:10.1038/s41467-018-07900-9.

[39] Q. Guo, C. Zhao, L.I. Escano, Z. Young, L. Xiong, K. Fezzaa, W. Everhart, B. Brown, T. Sun, L. Chen, Transient dynamics of powder spattering in laser powder bed fusion additive manufacturing process revealed by in-situ high-speed high-energy x-ray imaging, Acta Mater. 151 (2018) 169–180. doi:10.1016/j.actamat.2018.03.036.

[40] L.I. Escano, N.D.N.D. Parab, L. Xiong, Q. Guo, C. Zhao, K. Fezzaa, W. Everhart, T. Sun, L. Chen, Revealing particle-scale powder spreading dynamics in powder-bed-based additive manufacturing process by high-speed x-ray imaging, Sci. Rep. 8 (2018) 15079. doi:10.1038/s41598-018-33376-0.

[41] C.L.A. Leung, S. Marussi, M. Towrie, R.C. Atwood, P.J. Withers, P.D. Lee, The effect of powder oxidation on defect formation in laser additive manufacturing, Acta Mater. 166 (2019) 294–305. doi:https://doi.org/10.1016/j.actamat.2018.12.027.

[42] C. Zhao, K. Fezzaa, R.W. Cunningham, H. Wen, F. De Carlo, L. Chen, A.D. Rollett, T. Sun, Real-time monitoring of laser powder bed fusion process using high-speed X-ray imaging and diffraction, Sci. Rep. 7 (2017) 3602. doi:10.1038/s41598-017-03761-2.

[43] C.L.A. Leung, S. Marussi, R.C. Atwood, M. Towrie, P.J. Withers, P.D. Lee, In situ X-ray imaging of defect and molten pool dynamics in laser additive manufacturing, Nat. Commun. 9 (2018) 1355. doi:10.1038/s41467-018-03734-7.

[44] N.P. Calta, J. Wang, A.M. Kiss, A.A. Martin, P.J. Depond, G.M. Guss, V. Thampy, A.Y. Fong, J.N. Weker, K.H. Stone, C.J. Tassone, M.J. Kramer, M.F. Toney, A. Van Buuren, M.J. Matthews, An instrument for in situ time-resolved X-ray imaging and diffraction of laser powder bed fusion additive manufacturing processes, Rev. Sci. Instrum. 89 (2018) 55101. doi:10.1063/1.5017236.

[45] S.J. Wolff, H. Wu, N. Parab, C. Zhao, K.F. Ehmann, T. Sun, J. Cao, In-situ high-speed X-ray imaging of piezo-driven directed energy deposition additive manufacturing, Sci. Rep. 9 (2019) 962. doi:10.1038/s41598-018-36678-5.

[46] R. Cunningham, C. Zhao, N. Parab, C. Kantzos, J. Pauza, K. Fezzaa, T. Sun, A.D. Rollett, Keyhole threshold and morphology in laser melting revealed by ultrahigh-speed x-ray imaging, Science. 363 (2019) 849–852. doi:10.1126/science.aav4687.

[47] A.A. Martin, N.P. Calta, S.A. Khairallah, J. Wang, P.J. Depond, A.Y. Fong, V. Thampy, G.M. Guss, A.M. Kiss, K.H. Stone, C.J. Tassone, J. Nelson Weker, M.F. Toney, T. van

Buuren, M.J. Matthews, Dynamics of pore formation during laser powder bed fusion additive manufacturing, Nat. Commun. 10 (2019) 1987. doi:10.1038/s41467-019-10009-2.

[48] C. Kenel, D. Grolimund, X. Li, E. Panepucci, V.A. Samson, D.F. Sanchez, F. Marone, C. Leinenbach, In situ investigation of phase transformations in Ti-6Al-4V under additive manufacturing conditions combining laser melting and high-speed micro-X-ray diffraction, Sci. Rep. 7 (2017) 16358. doi:10.1038/s41598-017-16760-0.

[49] C. Kenel, D. Grolimund, J.L. Fife, V.A. Samson, S. Van Petegem, H. Van Swygenhoven, C. Leinenbach, Combined in situ synchrotron micro X-ray diffraction and high-speed imaging on rapidly heated and solidified Ti–48Al under additive manufacturing conditions, Scr. Mater. 114 (2016) 117–120. doi:10.1016/j.scriptamat.2015.12.009.

[50] R.W. Messler Jr, Principles of Welding, Wiley-VCH Verlag GmbH, Weinheim, Germany, 1999. doi:10.1002/9783527617487.

[51] S. Kou, C. Limmaneevichitr, P.S. Wei, Oscillatory Marangoni flow: a fundamental study by conduction-mode laser spot welding, Weld. J. 90 (2011) 229–240.

[52] M. Poletto, D.D. Joseph, Effective density and viscosity of a suspension, J. Rheol. (N. Y. N. Y). 39 (1995) 323–343. doi:10.1122/1.550692.

[53] P. Jin, H. Sumeng, W. Xingxing, W. Jiansheng, Z. Furong, Effect of filler metal on three-dimensional transient behavior of keyholes and molten pools in laser welding, Chinese J. Lasers. 45 (2018) 0102003. doi:10.3788/CJL201845.0102003.

[54] A. Paul, T. Debroy, Free surface flow and heat transfer in conduction mode laser welding,

Metall. Trans. B. 19 (1988) 851–858. doi:10.1007/BF02651409.

[55] P. Bidare, I. Bitharas, R.M. Ward, M.M. Attallah, A.J. Moore, Fluid and particle dynamics in laser powder bed fusion, Acta Mater. 142 (2018) 107–120. doi:10.1016/j.actamat.2017.09.051.

[56] B. Schoinochoritis, D. Chantzis, K. Salonitis, Simulation of metallic powder bed additive manufacturing processes with the finite element method: A critical review, Proc. Inst. Mech. Eng. Part B: J. Eng. Manuf. 231 (2017) 96–117. doi:10.1177/0954405414567522.

Highlights

- Developed the full-field melt flow mapping approach to study the detailed melt flow dynamics under additive manufacturing conditions
- Revealed the location-specific flow patterns in different regions of the melt pool and quantified the speeds of various types of flow
- Reconstructed three-dimensional flow pattern under both conduction-mode melting and depression-mode melting
- Experimentally analyzed the prevailing physical processes at different locations in the melt pool

In-situ full-field mapping of melt flow dynamics in laser metal additive manufacturing

Qilin Guo [a, b], Cang Zhao [c], Minglei Qu [a, b], Lianghua Xiong [b], S. Mohammad H. Hojjatzadeh [a, b], Luis I. Escano [a, b], Niranjan D. Parab [c], Kamel Fezzaa [c], Tao Sun [c, *], Lianyi Chen [a, b, **]

[a] Department of Mechanical Engineering, University of Wisconsin-Madison, Madison, WI 53706, USA

[b] Department of Mechanical and Aerospace Engineering, Missouri University of Science and Technology, Rolla, MO 65409, USA

[c] X-ray Science Division, Advanced Photon Source, Argonne National Laboratory, Lemont, IL 60439, USA

* Corresponding author

** Corresponding author

E-mail addresses: lianyi.chen@wisc.edu (Lianyi Chen), taosun@aps.anl.gov (Tao Sun)

Abstract

Melt flow plays a critical role in laser metal additive manufacturing, yet the melt flow behavior within the melt pool has never been explicitly presented. Here, we report in-situ characterization of melt-flow dynamics in every location of the entire melt pool in laser metal additive manufacturing by populous and uniformly dispersed micro-tracers through in-situ high-resolution synchrotron x-ray imaging. The location-specific flow patterns in different regions of the melt pool are revealed and quantified under both conduction mode and depression mode. The physical processes at different locations in the melt pool are identified. The full-field melt-flow mapping approach reported here opens the way to study the detailed melt-flow dynamics under real additive manufacturing conditions. The results obtained provide crucial insights into laser additive manufacturing processes and are critical for developing reliable high-fidelity computational models.

Keywords: Metal additive manufacturing, powder bed fusion, laser processing, melt flow, x-ray imaging

1. Introduction

Melt flow within the melt pool in laser metal additive manufacturing [e.g., laser powder bed fusion (LPBF), direct energy deposition (DED)] determines the heat transfer and mass transfer, thus plays a critical role in melt pool development [1], defect formation and evolution [2–8], solidification [9–11], and spatter generation [12–14]. Consequently, the melt flow behavior significantly affects the microstructures and properties of the additively manufactured parts [4,5,15–17]. Therefore, understanding the melt flow behavior in the melt pool is crucial for microstructure prediction and process control.

Due to the difficulty in experimentally visualizing the fluid flow inside the melt pool, extensive modelling and simulation work have been carried out to study the flow patterns under various conditions, i.e., with different laser power and scan speed that favors either depression-mode melting (a depression is formed in the melt pool under high power density due to the recoil pressure that caused by the intense material vaporization) or conduction-mode melting (a relatively shallow and wide melt pool is created under low power density without having a visible depression) [15,18]. Effect of surface active agent on melt flow was also studied by simulation [19]. However, given the complexity of the physics in laser additive manufacturing, it is extremely challenging to simulate the involved multi-physics phenomena using a single numerical model [20]. In fact, major assumptions must be applied in most of simulations [7,15,19–25]: some of assumptions are applied for the sake of calculation efficiency, some are made due to the unavailability of data, and the others are made because the underlying physics are still not well understood. All these assumptions will affect the accuracy of the models to certain extent. As a result, even though most of the models have been validated by comparing the simulated melt pool/track shape or size with post-mortem characterization results, the calculated melt flow results are not always consistent, and sometimes are even opposite. Discrepancies of the flow prediction were observed along the front depression wall [10,26,27], along the rear depression wall [13,18], along the bottom of melt pool [13,28], around the depression outlet [10,29], and behind the depression outlet [26,28]. Moreover, some physical mechanisms during laser processing under depression mode were interpreted with the more computation-efficient conduction-mode model, regardless of the essential distinction between the two melting modes. Thus, it is critical to experimentally unveil the melt flow behavior within the melt pool in laser additive manufacturing under both conduction-mode and depression-mode melting, for understanding the actual melt flow behavior and for developing and validating computational models.

Extensive work has been done in the welding community to characterize the liquid flow behavior in the melt pool by using flow tracers in the last few decades [3,4,12,14,16,26,30–37]. A very recent paper provides direct evidence of surface active element induced flow pattern reversion [38]. The tracers used in welding research are usually in relatively large size (50 μm – 500 μm) and small amount (≤ 80 counts per test), which can only trace melt flow behavior in certain area of the melt pool. Visible light imaging, such as glass flanking [4,35], were used to directly observe the flow pattern inside melt pool. However, the glass plate changes the heat transfer condition and cuts off the flow at the cross section, so that the observed flow pattern may differ from the real laser processing condition. Recently, in-situ x-ray imaging was used to study laser additive manufacturing processes [39–49]. The latest research [8] used tungsten particles to trace melt flow by synchrotron x-ray imaging, but only presented melt flow behavior in one projected view and in localized area of the melt pool.

Characterizing the three-dimensional melt flow in real laser additive manufacturing condition, especially under laser powder bed fusion condition, is much more challenging, because the laser usually scans in much higher speed and the resulting melt pool is much smaller. Due to the tremendous challenge, the melt flow behavior in the entire melt pool under real laser additive manufacturing conditions has not been unveiled.

In this work, we developed an approach to trace the melt flow behavior in the whole melt pool in laser additive manufacturing by uniformly dispersing populous micro-tracers (diameter of about 5 μm) and performing in-situ high-speed high-resolution x-ray imaging. We revealed the melt flow dynamics in every location of the entire melt pool under both conduction-mode and depression-mode melting, and analyzed the driving forces of liquid flow and the physical processes in the melt pool.

2. Materials and methods

2.1 Experimental setup

In-situ high-speed high-resolution x-ray imaging was used for direct observation of the melt pool dynamics from different views during laser scanning, as schematically shown in Fig. 1(a) and Supplementary Fig. 1. The synchrotron x-ray beam (Beamline 32-ID-B, Advanced Photon Source, Argonne National Laboratory) penetrated through the metal samples and the transmitted signal was captured by a detection system [39,40,42], which recorded the videos in this work with a frame rate of 140 kHz and a spatial resolution of 1.97 μm/pixel. A continuous-wave laser beam, with a wavelength of 1070 ± 10 nm and a maximum output power of 520 W, was used to melt the powder bed. Table 1 listed the materials and detailed processing parameters in this work. Each set of parameters was repeated three times. The parameter selection for generating conduction-mode melting and depression-mode melting is based on our previous work [1]. Powders with average diameter of 35 μm were manually spread on the substrate to form a powder bed with a layer thickness of 100 ± 10 μm by using a wiper made by weighing paper. Two setups were made, one where the laser beam scans perpendicular to the x-ray beam to get the longitudinal projection of the melt pool [as shown in Fig. 1(a) and Supplementary Fig. 1(a)], and another where the laser scans parallel to the x-ray to get the transverse projection of the melt pool [as shown in the inset of Fig. 1(a) and Supplementary Fig. 1(b)]. The three-dimensional coordinate system used in this study, as indicated on the powder bed in Fig. 1(a), was defined as follows: z is the normal direction of the powder bed, y is the laser scan direction, and x is the normal direction of y-z plane, following the right-hand rule.

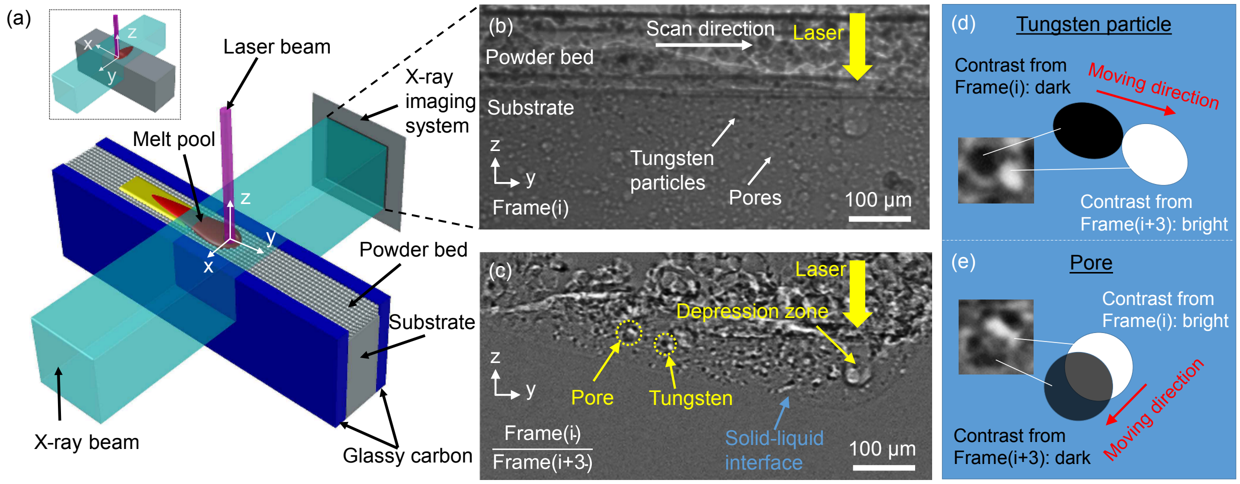

Fig. 1. Method for in-situ full-field mapping of melt flow dynamics. (a) Schematic illustration showing the in-situ x-ray imaging setup for laser powder bed fusion process. The high-speed high-resolution x-ray imaging system was used to capture the movement of tracing particles within the melt pool in the longitudinal view, as well as the transverse view (as illustrated by the simplified drawing in the inset). The x-y-z coordinate system used in this paper is indicated on the powder bed, where z is the normal direction of powder bed, y is the laser scan direction, and x is the normal direction of y-z plane, following the right-hand rule. (b) Representative x-ray image obtained at Frame(i). Uniformly dispersed populous micro-tracers (tungsten particles and pores) for melt flow tracing can be clearly identified from the x-ray image. (c) Representative x-ray image after image processing to show tracer movement and melt pool boundary. To obtain enhanced contrast, the image intensity at each pixel of Frame(i) is divided by the intensity of corresponding pixel in Frame(i+3). (d, e) Schematics showing different contrast of two types of tracers after image processing. For tungsten particle, the dark contrast comes from Frame(i) while the bright contrast comes from Frame(i+3). On the contrary, for pore, the bright contrast comes from Frame(i) and the dark contrast is from Frame(i+3). The insets in (d) and (e) are zoom-in views of the circled areas in (c).

Table 1 Materials and processing parameters

Material	Processing parameter	Melting mode
AlSi10Mg	260 W, 0.6 m/s	Conduction mode
AlSi10Mg	364 W, 0.6 m/s	Depression mode
Al-6061	520 W, 0.4 m/s	Depression mode

2.2 Materials

Two aluminum alloys, AlSi10Mg and Al-6061, were used for this study. Aluminum alloys are selected because of their high x-ray transparency. This study mainly focuses on AlSi10Mg, a widely used material for additive manufacturing. Al-6061, as a common aluminum alloy on market, was chosen to check whether the melt flow pattern observed in AlSi10Mg can also be observed in another alloy with different composition. The powder bed is composed of either AlSi10Mg or Al-6061 aluminum alloy, with the substrate material identical to the powders. To ensure better x-ray transparency, the powder bed width (along x-ray incidence) was fixed at 0.5 mm when the laser scans perpendicular to the x-ray beam (with a scan length of 2.5 mm), while 1.0 mm-thick substrates were used when the laser scan direction was parallel to the x-ray beam (with a scan length of 0.8 mm). Argon gas was used for process protection.

2.3 Flow tracing approach

Flow tracers were used to trace the melt flow during laser melting. The speed of a tracer was calculated by dividing its displacement by its travelling time. To be specific, the tracer's displacement was calculated through its 2-D coordinate change from one frame to the next in x-ray videos. The travelling time is the time interval between two frames, which was determined by the recording frame rate (140 kHz).

For the tracers to effectively indicate the movement of surrounding liquid flow, several requirements must be fulfilled: (1) The tracer must remain solid in the molten metal, meaning that tracer's melting temperature should be much higher than that of the matrix material (aluminum, in this case). (2) For the tracer to be detectable in x-ray images, the tracer must exhibit sharp contrast compared with matrix material, which means the tracer's density should be either much higher or lower than the matrix material. (3) The gravity/buoyancy of the tracer should have negligible effect on its movement. (4) The tracer must be accelerated fast enough by the surrounding liquid to avoid noticeable delay to the flow. (5) The tracer should not significantly change the viscosity of the molten liquid in the melt pool. 1 vol.% tungsten micro-particles (with an average diameter of 5 μm) in metal powders were identified as the main tracers to fulfill all the above requirements. The detailed analysis will be presented in the **Discussion** section.

The tungsten micro-particles were uniformly mixed with the feedstock aluminum powders by ball milling. Both size and amount of the tracer particles were optimized to be able to trace the melt flow in every location of the whole melt pool, yet impose minimum effect on the viscosity of the molten aluminum. Also, the small tracers used here allowed us to embed a large number of tracers under a fixed volume fraction, so that the fluid flow in every location of the melt pool could be traced accurately.

Uniformly dispersed micro-sized pores in AlSi10Mg were used as a complementary tracer, as marked in Fig. 1(b). The pores in the AlSi10Mg sample were introduced in LPBF building process. The mass density of pore is much lower than that of aluminum melt, which is used to cross-check the effect of the tracer density on melt flow tracing results. The pore movement in the main body of the melt pool was consistent with the tungsten particle movement, except for the region around depression zone (the reason for the discrepancy is explained in the **Discussion** session).

2.4 Image processing

To clearly identify the melt pool boundary and tracer movement, the raw x-ray images were processed by ImageJ to reduce noise and enhance contrast. The image intensity at each pixel of Frame(i) was divided by the intensity of corresponding pixel in Frame(i+3), so that the motionless part in the image was converted to blank background. The representative post-processed image is shown in Fig. 1(c), where the tracer movement is much clearer and the melt pool boundary is obvious. Note that the projection position of a particular tracer in Frame(i) and Frame(i+3) will both appear in a processed image, but the resulting contrasts are different for each type of tracer. For tungsten particle, the resulting contrast from Frame(i) appears to be dark in the processed image, while the resulting contrast from Frame(i+3) is bright, as illustrated in Fig. 1(d). As for the pore, the contrast from Frame(i) is bright but the contrast from Frame(i+3) is dark, as shown in Fig. 1(e).

3. Results

Different flow patterns were observed between the conduction-mode melting and depression-mode melting, due to their distinct forming mechanisms. In conduction-mode melting (also referred to as melt-in mode in welding community [50]), the material is heated up from its surface and the energy being deposited exceeds the rate at which heat is being conducted away, so that the temperature eventually reaches the melting point to form a melt pool. Under depression-mode melting, the energy from the heat source is so intense that the temperature in the material not just exceeds the melting point but reaches the boiling point. In this case, the intensive vaporization of the material applies a recoil pressure to the melt pool, thus creates a depression zone. In the welding community, the depression mode is also called "keyhole mode" when the depression zone dimension ratio (depth over half width) is larger than 1, and "transition mode" when the ratio is less than 1. Under depression mode, the heat source not just heats up the top surface of the material, but also heats up the inside of material through the depression zone. Owing to the different physics underpinning these two melting modes, the melt flow behaviors appear very differently, as detailed in the following two sections.

3.1 Melt flow pattern under conduction-mode melting

The general shape of the melt pool under conduction mode in both longitudinal view (projected in y-z plane) and transverse view (projected in x-z plane) are displayed in Figs. 2(a) and 2(c), respectively, with the melt pool boundary marked by yellow dashed line. The test was on AlSi10Mg powder bed with a laser power of 260 W and a scan speed of 0.6 m s^{-1}. The representative tracers are circled in the image, with their projectional moving directions in y-z plane indicated by arrows. The moving trend of the tracers is summarized in the corresponding schematics shown in Figs. 2(b) and 2(d). In transverse view, as displayed in Fig. 2(c), the tracers in the center plane of the melt pool move upward, while those close to the melt pool sidewalls move downward. Two vortices are thus formed with opposite circulating directions, as illustrated in Fig. 2(d). In longitudinal view [Fig. 2(a)], arrows in yellow and blue were used to distinguish the movement of tracers in the center plane and along the sidewalls. As depicted in Fig. 2(b), the flow forms a clockwise vortex ① ahead of the laser beam and a counterclockwise vortex ② behind the laser beam. The projectional flow speed (the projection of the flow velocity in the y-z plane) of three representative streams, A, B, and C will be quantified in section 3.2. The flow along the sidewalls in longitudinal view, as indicated by blue arrows in Fig. 2(b), travels from the top surface to the bottom of the melt pool, which is consistent with the observation in the transverse view [Fig. 2(c)]. A demonstration shows how the flow trend (slightly behind laser beam) shifts between the longitudinal view and the transverse view is displayed in Supplementary Movie 1. A three-dimensional reconstruction for conduction-mode melt flow is exhibited in Fig. 2(e), based on the observations above. For the clarity of illustration, the melt pool is displayed in halves, with one half (colored by cyan, transparent) showing the three-dimensional flow inside the melt pool, and the other half (colored by gray, opaque) showing the two-dimensional flow pattern only in the middle cross-section (y-z plane). The arrows in black display the flow on the top surface of melt pool, while the yellow arrows show the flow in the center plane, and the blue arrows represent the flow along the melt pool sidewalls. Different views of the three-dimensional melt flow in the whole melt pool can be found in Supplementary Movie 2.

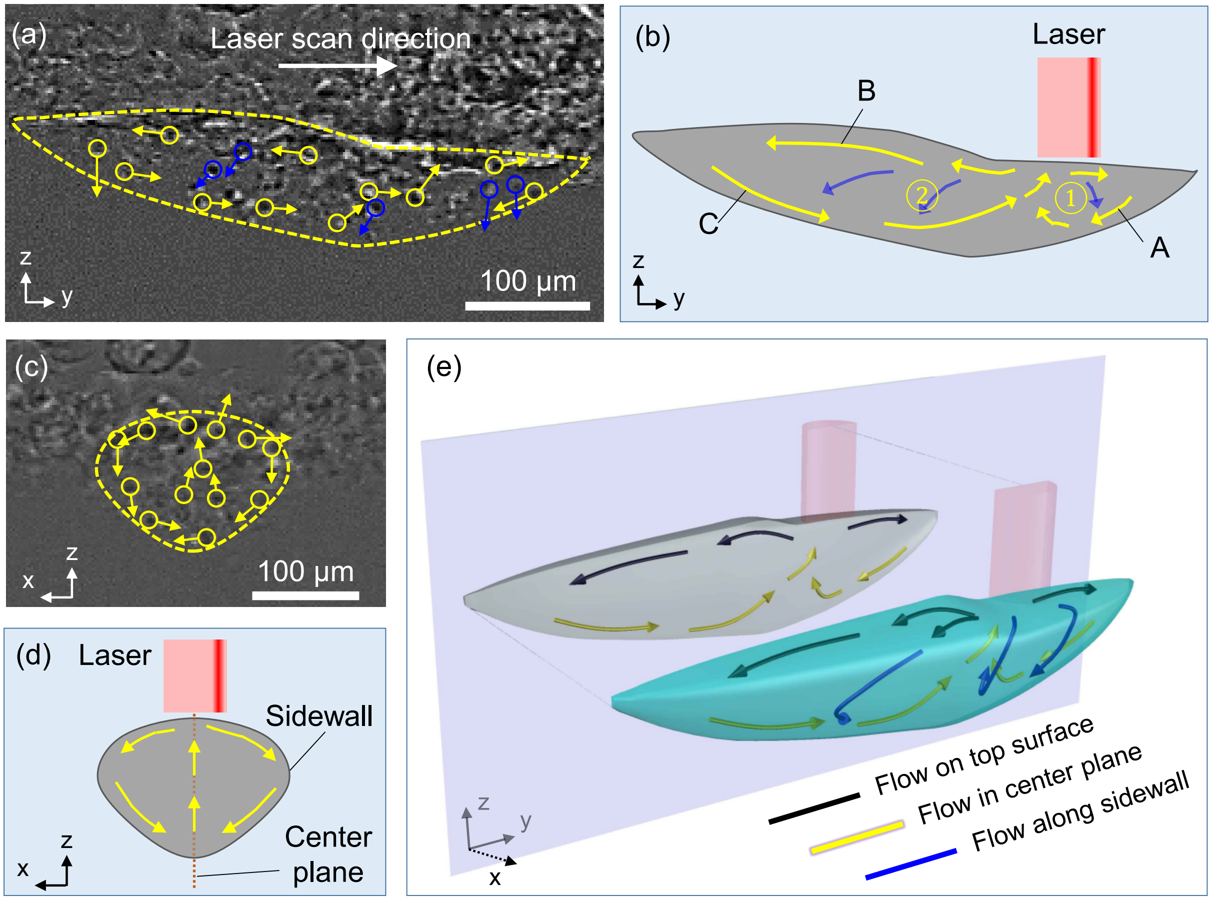

Fig. 2. Melt flow behavior under conduction mode. (a) X-ray image showing the instantaneous liquid flow direction in y-z projection plane (longitudinal view). (b) Schematic summarizing the melt flow pattern in y-z projection plane. (c) X-ray image showing the instantaneous liquid flow pattern in x-z plane (transverse view). (d) Schematic summarizing the melt flow pattern in x-z projection plane. (e) Reconstruction of three-dimensional melt flow pattern. All the tests were carried out on AlSi10Mg powder bed with a laser power of 260 W and a laser scan speed of 0.6 m s^{-1}. The laser D4σ diameter is around 80 μm.

3.2 Melt flow pattern under depression-mode melting

With the formation of depression, the laser beam directly interacts with the interior of melt pool, which promotes the energy absorption that leads to much larger melt pool with more complex flow pattern as compared with that under conduction mode. To facilitate the description, the melt pool is divided into three regions [i.e., tail, body, and head, as shown in Figs. 3(a)-3(c), respectively] along the laser scan direction. The arrows in yellow and blue, similar to conduction mode, were used to distinguish the tracer motions in the center plane and along the sidewalls. In the transverse view of melt pool, to differentiate the flow patterns around the depression from those in the body of melt pool (behind depression), the flow behavior was recorded during laser scanning [Fig. 3(e)] and 50 μs after the laser was off [before the contraction of the melt pool boundary, as displayed in Fig. 3(g)], respectively. Note that t_o is the moment when the laser was turned off.

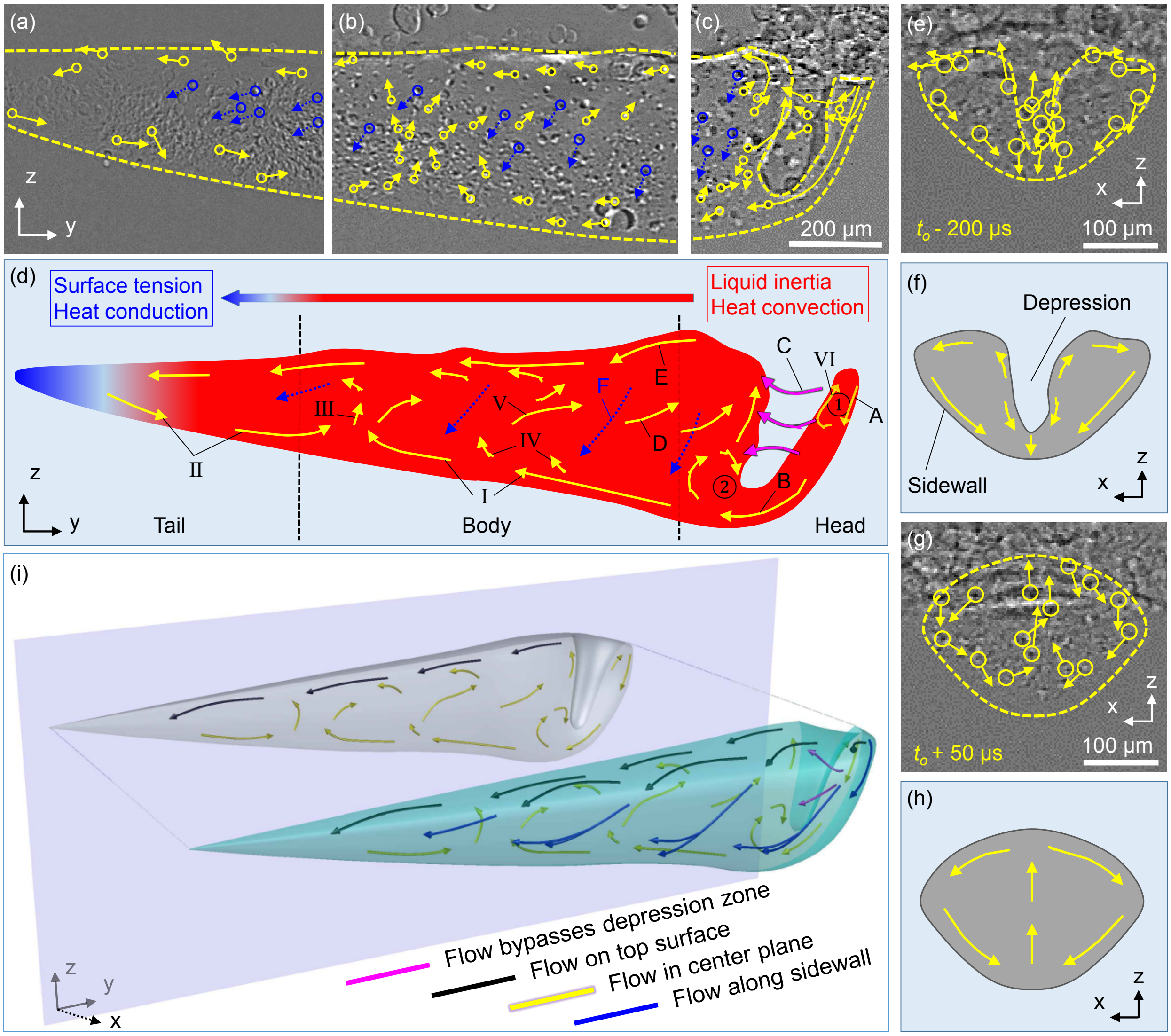

Fig. 3. Melt flow behavior under depression mode. (a)-(c) X-ray images showing the instantaneous liquid flow direction in y-z projection plane. (d) Schematic summarizing the flow pattern in y-z projection plane. (e), (g) X-ray images displaying the flow pattern around depression zone (e) and behind depression zone (g) in x-z projection plane. (f), (h) Schematics summarizing the flow pattern around depression zone (f) and behind depression zone (h) in x-z projection plane. (i) Reconstruction of three-dimensional melt flow pattern under depression mode. The tests were carried out on AlSi10Mg powder bed with 364 W laser power and 0.6 m s^{-1} scan speed. t_o is the moment when the laser was turned off.

The trend of tracer motions in Figs. 3(a)-3(c) is summarized and combined together in the schematic Fig. 3(d), while the tracer movement in Fig. 3(e), 3(g) are depicted in schematic Figs. 3(f), 3(h). Six types of flow that marked by A-F in Fig. 3(d) will be quantified in section 3.3.

In the center plane, as shown in Fig. 3(d), the flow around the depression moves upward near the depression outlet, while moves downward near the bottom of depression, which is consistent with the flow pattern around the depression in transverse view [Fig. 3(f)]. The flow bypasses the depression travels in the opposite direction to the laser scan direction, as illustrated by flow C in Fig. 3(d). The flow near the melt pool surface moves backward, from depression outlet to the tail of melt pool. The flow at the bottom of melt pool (flow I) also has a main trend of moving backward, except a short forward flow (flow II) was observed at the rear bottom of melt pool. Flow I and II collide to form a merged flow (flow III) which moves upwards and splits into flows of opposite directions. In the area between the top and bottom backward flow, as pointed out by flow D in Fig. 3(d), the general flow movement in the center plane have a tendency of going forward and upward, which is consistent with the observation of flow pattern in transverse view [Fig. 3(h)]. The flow along the sidewalls of the melt pool moves downward, as displayed by the blue arrows in Fig. 3(d), which is in accordance with the transverse-view observations in Figs. 3(f), 3(h). Two movies (Supplementary Movies 3, 4) were made to demonstrate the flow pattern transition (around depression and behind depression) between the longitudinal view and transverse view. A three-dimensional reconstruction of depression-mode melt flow is shown in Fig. 3(i). The arrows in magenta show the flow bypasses the depression, while the black arrows display the flow on the top surface of melt pool, the yellow arrows show the flow in the center plane, and the blue arrows represent the flow along the melt pool sidewalls. The different views of the three-dimensional melt flow in the whole melt pool is shown in Supplementary Movie 5.

To confirm that the above melt flow pattern is not limited to an alloy with a specific composition, tests on Al-6061 were carried out. Very similar melt flow pattern in depression-mode melting was observed, as displayed in Fig. 4.

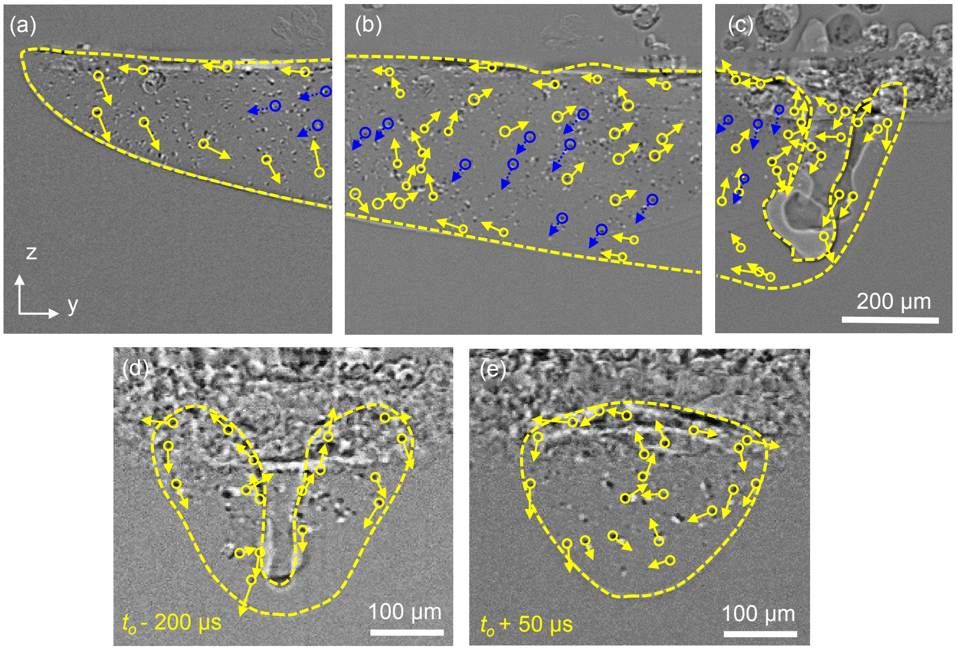

Fig. 4. Melt flow pattern in Al-6061. (a-c) X-ray images showing the instantaneous liquid flow direction in y-z projection plane. (d, e) X-ray images displaying the flow pattern around depression zone (d) and behind depression zone (e) in x-z projection plane. The tests were carried out on Al-6061 powder bed with 520 W laser power and 0.4 m/s scan speed.

3.3 Quantification of flow speed

The projectional speed of melt flow A, B, C [as marked in Fig. 2(b)] under conduction mode and flow A, B, C, D, E, F [as marked in Fig. 3(d)] under depression mode were measured and shown in Figs. 5(a), 5(b), respectively. The flow direction and location were detailed in Table 2. Note that the flow E, D, F in depression mode were only quantified within a 300 μm region after the depression (as we will show later in Fig. 6 that the flow speed attenuates fast at the tail of melt pool). Since the tracers at different locations (e.g., in the center vs. near the edge) of a particular flow stream may have different speeds, the average speeds of each type of flow and the standard deviations are calculated and displayed by blue bars. In addition, the maximum speeds of each type of flow are shown in the histograms by red bars as a useful measure, given that the three-dimensional motion of the tracers may have components perpendicular to view plane. Under both conduction mode and depression mode, flow A (downward flow along the front melt pool boundary) has the highest speed, with maximum speed values of 2.83 m s^{-1} for conduction mode and 3.68 m s^{-1} for depression mode.

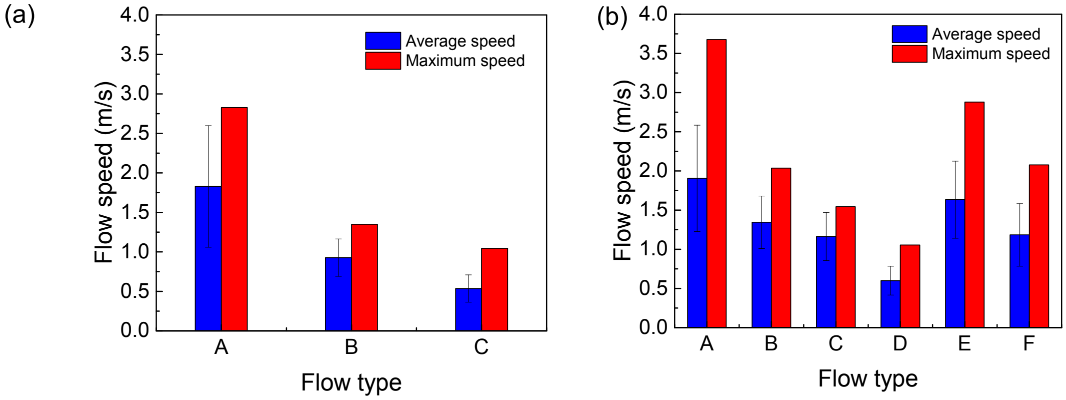

Fig. 5. Quantification of flow speed under conduction mode (a) and depression mode (b) as a function of flow type. The flow types A, B, and C under conduction mode were marked in Fig. 2(b). The flow types A-F under depression mode were indicated in Fig. 3(d).

Table 2. Types of flow and their locations

Melting mode	Flow type	Flow direction	Flow location
Conduction	A	Backward	Along the front melt pool bottom
	B	Backward	Along the melt pool surface
	C	Forward	Along the rear melt pool bottom
Depression	A	Downward	Along the front depression wall
	B	Downward & backward	Along the depression bottom
	C	Backward	Around the depression zone
	D	Upward & forward	Toward the depression outlet
	E	Backward	Along the surface of melt pool
	F	Downward & backward	Along the sidewall of melt pool

The above measurements provide speed information of each type of flow in localized regions. Further quantification was carried out to analyze the general trend of the flow speed as a function of location across the melt pool. Quantification was first carried out on AlSi10Mg [Figs. 6(a), 6(b)] and then on Al-6061 [Figs. 6(c), 6(d)]. From the middle of rear depression wall [as marked by red dot in Fig. 6(a)], the melt pool behind the reference position was divided into 12 sections with 100 μm segment width. The projectional speed of the tracers in each section (Y_i) were measured and plotted in Fig. 6(b). Both the average speed and maximum speed exhibit a general decreasing trend as a function of the distance from depression. In the first section Y_1, the average speed is 0.52 m/s and the maximum speed is 1.25 m/s. In the last section Y_{12}, the average speed is 0.08 m/s and the maximum speed is 0.15 m/s, which are both an order of magnitude lower than those in section Y_1. The quantification stopped at Y_{12} because the flow speed is so low that approaches the measurement precision (0.025 m/s). The same quantification strategy was applied to Al-6061 melt pool, as shown in Fig. 6(c). Similar decreasing trend of the speeds were observed, as shown in Fig. 6(d).

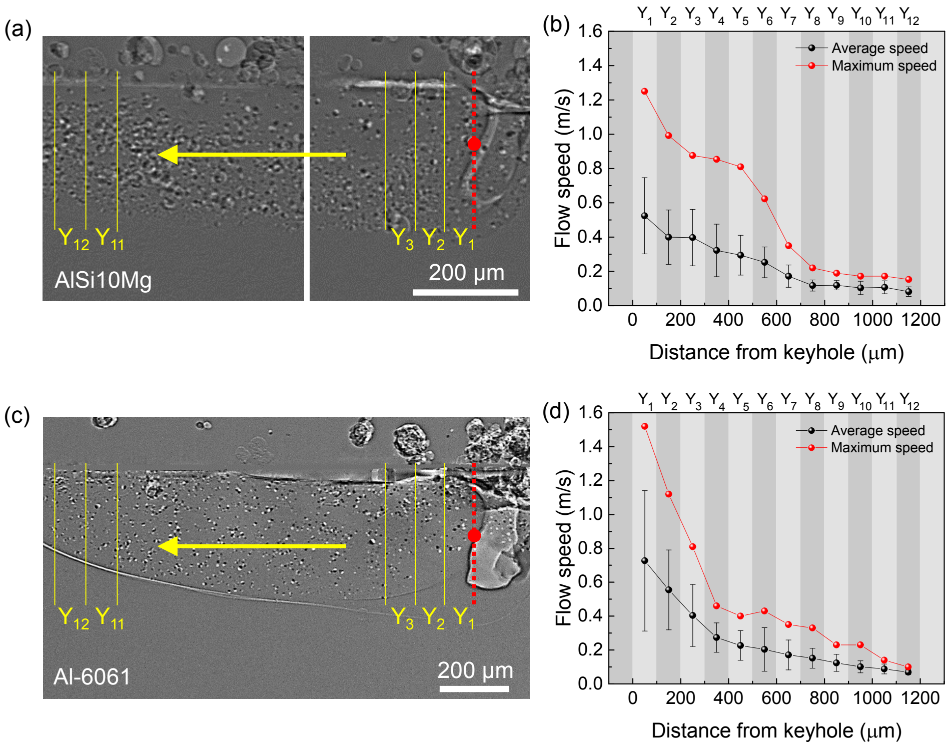

Fig. 6. Quantification of flow speed along melt pool. (a) X-ray image illustrating the quantification method of flow speed as a function of location behind depression zone. Note that two images were jointed together here to display the full quantification length. The test was carried out on AlSi10Mg. The middle of rear depression wall was set as the reference point. The projectional flow speeds in the rest part of melt pool were averaged in consecutive sections with an increment of 100 μm. (b) The measured average and maximum projectional flow speed as a function of location. (c, d) Quantification of flow speed in Al-6061 melt pool.

Due to the highly dynamic nature of the depression zone, the general flow speed ahead of rear depression wall was not quantified in the above analysis. Instead, a particular tracer that moved all the way down in the thin liquid film ahead of depression zone was tracked to reveal the flow behavior at the depression area, as displayed in Fig. 7(a). This tracer is special, because its trajectory is rarely seen during the experiments. As illustrated in Fig. 3(d), if a tracer wants to move all the way down along the liquid film ahead of the depression, it needs to experience flow A and then flow B. However, due to the coaction of the vortex ① and the strong side flow C, most tracers entering the depression front will be dragged to other directions, and only the ones happen to be at the exact center of the depression front film could continue to flow downward, as illustrated by the inset in Fig. 7(b). Therefore, the tracer that was tracked in Fig. 7(a) must have moved in the y-z plane with minimum speed component in x-direction. This tracer's speed can then reflect the real speed of downward flow ahead of the depression zone. Fig. 7(b) indicates that its speed dropped dramatically in the liquid film ahead of depression zone, decreasing by around 90% from 4.5 m s^{-1} (0 μs) to 0.45 m s^{-1} (64 μs), and then became relatively stable when it entered the main body of the melt pool.

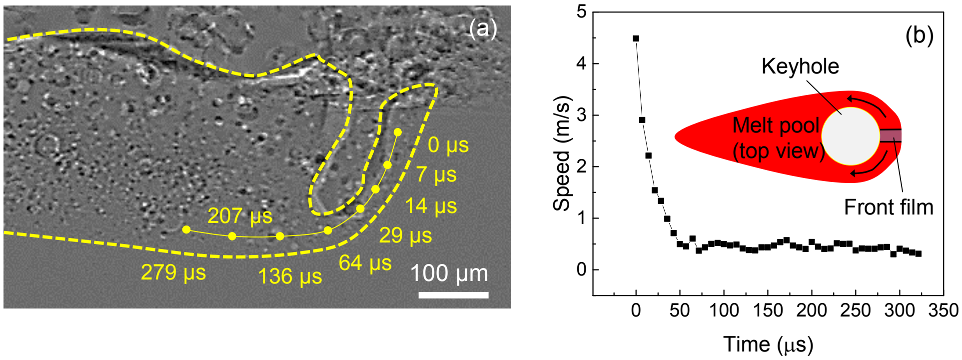

Fig. 7. Quantification of flow speed along front depression wall. (a) X-ray image displaying the trajectory of a tracing particle travelling along front depression wall. The test was done on AlSi10Mg powder bed. Note that the yellow dot size in the image does not represent the real size of the tracing particle. (b) The speed of tracing particle as a function of time.

4. Discussion

4.1 Validity of flow tracing by tracer particles

To examine the effect of gravity/buoyancy on tracer movements, the settling velocity (v_p) of tungsten particle in liquid AlSi10Mg was calculated to be $v_p = 1.3\times10^{-4}$ m s^{-1} by the Stokes's law [51,52] (the detailed calculation is in Supplementary Note 1). The settling velocity is the terminal velocity for a free-fall particle in the liquid that only has gravity, buoyancy, and friction force on it. The calculated settling velocity is at least two orders of magnitude lower than the flow speeds measured in this work, meaning that the detected tracer speed must under strong influence from surrounding flow, otherwise their velocity will be closer to the settling velocity. To further confirm that the high-density tungsten micro-tracer does not influence the tracing results in our work, gas pores (almost zero density) are used as complementary tracers. Our results show that the pore movement in the main body of the melt pool is consistent with the tungsten particle movement. However, pores cannot be used as melt flow tracers in the depression region. The mechanism for this discrepancy was recently reported in [8].

To examine whether the tracer can be accelerated fast enough by the surrounding liquid, the tracer in Fig. 7(a) was investigated as an example because it entered into the front depression wall, where the flow moves the fastest (> 4.5 m/s) among the melt pool. Assuming the particle was accelerated to the maximum speed within one frame (~ 7 μs), the maximum acceleration of the tracer can be calculated to be 6.4×10^5 m s^{-2}, which is equivalent to a force of 0.81 μN by Newton's second law. However, the maximum drag force provided by the molten aluminum flow, by the Schiller-Naumann drag law [34], is calculated to be 4.2 μN (see Supplementary Note 2 for details), which can provide the particle with an acceleration of 5 times as much as it really needs. It was calculated that the tungsten particle can be accelerated to over 50% of the surrounding flow speed within 1.4 μs (see Supplementary Note 2 for details). Furthermore, within one frame (~7 μs), the tracer speed can be accelerated to over 85% of the flow speed. Since the motion delay between the micro-tracer particle (5 μm in size) and the surrounding flow is negligible, the tracers' movement can indeed reflect the liquid flow in the present experimental conditions.

To examine the effect of tracers on the viscosity of the liquid, it is calculated that the liquid with 1 vol.% tracer particles has a viscosity of 2.6% higher than the one without particles (see Supplementary Note 3 for details). In practice, the viscosity will increase less than 2.6% because the tracer concentration in the liquid will be lower than 1 vol%, considering that the substrate does not contain tracer particles before melting. Besides, none of the experiments exhibited significant local particle density variation, e.g. clusters or aggregations, in the melt pool. Thus, mixing 1 vol.% tungsten particles into feedstock powder will not significantly alter the viscosity of the melt and the flow pattern in the melt pool.

4.2 Analysis of driving forces for liquid flow in melt pool

The complex flow patterns revealed in this work have not been completely replicated by the models and simulations published so far. To understand the physics underlying melt flow pattern, the driving forces in the melt pool that account for the various flow patterns observed in different regions are analyzed below.

There are five major driving forces in the melt pool. Marangoni force drives the flow from high temperature region to low temperature region for a material with a negative temperature coefficient of surface tension (from low surface tension region to high surface tension region, most metals and alloys exhibit negative temperature coefficient of surface tension) [4,21,38,53,54]. Vaporization induced recoil pressure exerts an inward pressure normal to the vaporization surface [6,30]. High-speed vapor plume (can reach 10^2-10^3 m s^{-1} [55]) can induce shear force through friction at the liquid-gas interface [33,53]. Hydraulic pressure can exchange energy by either pressure (hydrostatic pressure) or by momentum (hydrodynamic pressure) [5]. Buoyance force drives liquid along density gradient [5,18,26]. The details about each type of driving forces can be found in Supplementary Notes 4-7.

In conduction-mode melt pool, the dominating driving force is Marangoni force, which drives the melt flow from hotter region to cooler region (the materials we studied have negative temperature coefficient of surface tension), i.e., from laser heating spot to melt pool rim. Therefore, in longitudinal view [Fig. 2(b)] the surface flow ahead of laser beam moves forward, while the one behind laser beam moves backward. When the flows reach each rim of melt pool, they will flow downward and return to the laser heating spot under the effect of hydraulic pressure. Thus, two close loops are formed: a clockwise loop ahead of laser beam and a counterclockwise loop behind the laser beam. Driven also by Marangoni force, the flows in transverse view [Fig. 2(d)] form another two close loops (consistent with recent research [38]), following a similar mechanism as in longitudinal view.

The flow pattern in depression-mode melt pool is rather complex, due to the intense vaporization induced depression zone. The vaporization-related forces, i.e., the recoil pressure and the vapor plume friction, dominate the flow pattern around the depression [the “Head” region in Fig. 3(d)]. The flow around the upper part of depression moves upward under Marangoni force [28] and the vapor plume friction [14,30], while the flow close to the bottom of depression moves downward due to the recoil pressure, as can be seen in both longitudinal view [Fig. 3(d), flow B] and transverse view [Fig. 3(f)]. The flow bypasses the depression zone is mainly driven by hydraulic pressure gradient, as a high-hydraulic pressure region is formed in the liquid film ahead of depression zone while the front depression wall keeps “pressing” the front liquid during its travelling. Note that the upward flow VI in vortex ① may temporarily disappear or enhance, which is hypothesized to be depending on the competition between the downward recoil pressure and the upward vapor plume friction on the front depression wall [30,33,53]. With the proceeding of depression zone, a low hydraulic-pressure region forms behind the bottom of depression [25], which drains the surrounding liquid into this region and thus induces the vortex ②. For the “Body” part of melt pool, as shown in Fig. 3(d), the surface flow moves backward from high temperature region to low temperature region (Marangoni force), similar to the condition of conduction-mode melting. The flow at the bottom (flow I) inherits the momentum from flow B and thus moves backward. Being freshly heated up at the depression, the flow I carries higher temperature liquid (with lower density) than those in the upper level within the melt pool. Therefore, the molten metal in flow I floats up (flow IV) under the buoyancy force during the backward transportation. The flow in the middle level of melt pool (flow D and V), aside from the upward movement, has a main tendency of moving forward, attracted by the low hydraulic pressure region around depression zone induced by the high-speed flows under Bernoulli's effect. At the "Tail" region of melt pool, the backward flow on the surface is driven by Marangoni force, while the flow II is generated when the surface flow bounces back at the melt pool rim. During the colliding of flow I and II, the momentum transfers from flow I and II to their merged flow—flow III.

4.3 Analysis of physical processes in the melt pool

Based on the quantitative analysis provided above, physical processes associated with kinetic energy damping and heat transfer are analyzed at different locations in the melt pool.

4.3.1 Liquid momentum versus surface tension

The extent of damping the flow, especially on the surface (mainly dominated by Marangoni convection), can be expressed by Weber number (We) as

$$We = \frac{\rho v^2 L}{\sigma} \tag{1}$$

where ρ is the liquid density, v is the flow speed, L is the characteristic length, and σ is the surface tension [23]. The Weber number is calculated to be $We = 1.78$ near the depression zone and $We = 0.007$ near the melt pool tail. It means that the inertia of the liquid overcomes the surface tension near depression region (where Marangoni convection/recoil pressure is strong), then becomes much less important when approaching the tail of the melt pool, as schematically shown in Fig. 3(d). Consequently, the melt pool surface at the head of melt pool is more rippled, caused by the momentum of upward liquid along the rear depression wall, while the surface at the tail of melt pool is rather flat and smooth because the surface tension will damp out the surface wave.

4.3.2 Heat conduction versus heat convection

To improve the computing efficiency and speed, some simplified modelling work (based on heat transfer theories) on laser processing choose to only consider the effect of heat conduction while neglect the effect of heat convection [13,56]. Here we show that the heat convection should not be neglected, as it is significant near the head of melt pool. With the measured flow speed, the relative effect of heat convection over heat conduction can be evaluated by the Péclet number (Pe), which is the product of Reynolds number (Re_L) and Prandtl number (Pr) as

$$Pe = Re_L \cdot Pr = \frac{\rho v L}{\mu} \cdot \frac{c_p \mu}{k} = \frac{Lv}{\alpha} \tag{2}$$

where L is the characteristic length, v is the local flow speed, and α is the thermal diffusivity. Taking the test in Fig. 6(a) as an example, $v = 1.25$ m s^{-1}, $\alpha = 6.6\times10^{-5}$ m^2 s^{-1} in section Y_1 near the depression zone; and $v = 0.08$ m s^{-1}, $\alpha = 3.54\times10^{-5}$ m^2 s^{-1} in section Y_{12} near the tail of melt pool. The characteristic length (L) is chosen as the hydraulic diameter (D_h) of the melt pool. In section Y_1, $L = D_h = 539$ µm; in section Y_{12}, $L = D_h = 427$ µm. (Method to calculate the hydraulic diameter is detailed in Supplementary Note 8.) The Péclet number is calculated to be $Pe_{(head)} = 10.2$ at the head of melt pool and $Pe_{(tail)} = 0.9$ at the tail. When $Pe \geq 10$, qualitatively, heat convection is considered to make a greater contribution to the thermal energy transportation [12]. The results indicate a strong heat convection could occur at the head of melt pool while heat conduction is dominating at the tail of melt pool. The prevailing physical processes along the melt pool were indicated in Fig. 3(d).

4. Conclusions

In the present work, for the first time, we revealed and quantified the melt flow dynamics in every location of the entire melt pool in laser metal additive manufacturing process under both conduction-mode and depression-mode melting. The major conclusions are detailed below:

(1) We developed a full-field melt flow mapping method to reveal the detailed melt flow dynamics under laser metal additive manufacturing conditions by tracing uniformly dispersed populous micro-tracers through in-situ high-speed high-resolution x-ray imaging.

(2) The melt flow behaviors were revealed in every location of the whole melt pool under both conduction-mode and depression-mode melting in laser additive manufacturing process. The conduction-mode melt pool possesses a simple flow pattern that is mainly driven by the Marangoni effect, while the flow pattern in depression-mode melt pool is rather complex, under the coaction of multiple driving forces. The flow pattern and flow speed are location dependent. The detailed (projectional) flow speeds in different regions of the melt pool under both conduction-mode and depression-mode melting were quantified in terms of average speed and maximum speed. Decreasing of the flow speed from the depression zone to the melt pool tail was observed and statistically analyzed.

(3) The driving forces for different types of melt flow were analyzed. Marangoni effect accounts for the flow movement from high-temperature region to low-temperature region (for a material with a negative temperature coefficient of surface tension) on the surface of the melt pool. Vaporization dominates the fluid flow along depression-zone walls. Hydraulic pressure

drives fluid flow from high-pressure region to low-pressure region. Buoyance force accounts for liquid convection from low-density region to high-density region.

(4) The prevailing physical processes concerning kinetic energy damping and heat transfer at the head of melt pool were experimentally identified to be liquid inertia and heat convection, respectively; while at the tail of melt pool, correspondingly, the physical processes were determined to be surface tension and heat conduction.

The full-field melt flow mapping approach reported here opens the way to study the melt flow dynamics under real additive manufacturing conditions. Our findings reported here are critical for not only understanding the laser additive manufacturing process and other laser processes, but also for developing reliable high-fidelity computational models.

Acknowledgements

The authors would like to thank Alex Deriy at the APS for his help on the beamline experiments. Q.G., M.Q., L.X., S.M.H.H., L.I.E., and L.C. acknowledge the financial support by National Science Foundation (Award No. 1762477). C.Z., N.D.P., K.F, and T.S. thank the Laboratory Directed Research and Development (LDRD) funding from Argonne National Laboratory, provided by the Director, Office of Science, of the U.S. Department of Energy under Contract No. DE-AC02-06CH11357. This research used resources of the Advanced Photon Source, a U.S. Department of Energy (DOE) Office of Science User Facility operated for the DOE Office of Science by Argonne National Laboratory under Contract No. DE-AC02-06CH11357.

References

[1] Q. Guo, C. Zhao, M. Qu, L. Xiong, L.I. Escano, S.M.H. Hojjatzadeh, N.D. Parab, K. Fezzaa, W. Everhart, T. Sun, L. Chen, In-situ characterization and quantification of melt

pool variation under constant input energy density in laser powder bed fusion additive manufacturing process, Addit. Manuf. 28 (2019) 600–609. doi:10.1016/j.addma.2019.04.021.

[2] Y. Kawahito, M. Mizutani, S. Katayama, Elucidation of high-power fibre laser welding phenomena of stainless steel and effect of factors on weld geometry, J. Phys. D. Appl. Phys. 40 (2007) 5854–5859. doi:10.1088/0022-3727/40/19/009.

[3] S. Katayama, Y. Kawahito, M. Mizutani, Elucidation of laser welding phenomena and factors affecting weld penetration and welding defects, Phys. Procedia. 5 (2010) 9–17. doi:10.1016/j.phpro.2010.08.024.

[4] F. Tenner, B. Berg, C. Brock, F. Klämpfl, M. Schmidt, Experimental approach for quantification of fluid dynamics in laser metal welding, J. Laser Appl. 27 (2015) S29003. doi:10.2351/1.4906302.

[5] B. Chang, C. Allen, J. Blackburn, P. Hilton, D. Du, Fluid flow characteristics and porosity behavior in full penetration laser welding of a titanium alloy, Metall. Mater. Trans. B. 46 (2015) 906–918. doi:10.1007/s11663-014-0242-5.

[6] I. Eriksson, J. Powell, A.F.H. Kaplan, Melt behavior on the keyhole front during high speed laser welding, Opt. Lasers Eng. 51 (2013) 735–740. doi:10.1016/j.optlaseng.2013.01.008.

[7] S. Shrestha, S. Rauniyar, K. Chou, Thermo-fluid modeling of selective laser melting: single-track formation incorporating metallic powder, J. Mater. Eng. Perform. 28 (2019) 611–619. doi:10.1007/s11665-018-3574-5.

[8] S.M.H. Hojjatzadeh, N.D. Parab, W. Yan, Q. Guo, L. Xiong, C. Zhao, M. Qu, L.I. Escano, X. Xiao, K. Fezzaa, W. Everhart, T. Sun, L. Chen, Pore elimination mechanisms during 3D printing of metals, Nat. Commun. 10 (2019) 3088. doi:10.1038/s41467-019-10973-9.

[9] K.N. Kowal, S.H. Davis, Strong shear-flow modulation of instabilities in rapid directional solidification, Acta Mater. 164 (2019) 464–472. doi:10.1016/j.actamat.2018.10.054.

[10] Y. Zhao, Y. Koizumi, K. Aoyagi, D. Wei, K. Yamanaka, A. Chiba, Molten pool behavior and effect of fluid flow on solidification conditions in selective electron beam melting (SEBM) of a biomedical Co-Cr-Mo alloy, Addit. Manuf. 26 (2019) 202–214. doi:10.1016/j.addma.2018.12.002.

[11] T. DebRoy, H.L. Wei, J.S. Zuback, T. Mukherjee, J.W. Elmer, J.O. Milewski, A.M. Beese, A. Wilson-Heid, A. De, W. Zhang, Additive manufacturing of metallic components – Process, structure and properties, Prog. Mater. Sci. 92 (2018) 112–224. doi:10.1016/j.pmatsci.2017.10.001.

[12] Y. Kawahito, Y. Uemura, Y. Doi, M. Mizutani, K. Nishimoto, H. Kawakami, M. Tanaka, H. Fujii, K. Nakata, S. Katayama, Elucidation of the effect of welding speed on melt flows in high-brightness and high-power laser welding of stainless steel on basis of three-dimensional X-ray transmission in situ observation, Weld. Int. 31 (2017) 206–213. doi:10.1080/09507116.2016.1223204.

[13] S.A. Khairallah, A.T. Anderson, A. Rubenchik, W.E. King, Laser powder-bed fusion additive manufacturing: Physics of complex melt flow and formation mechanisms of pores, spatter, and denudation zones, Acta Mater. 108 (2016) 36–45. doi:10.1016/j.actamat.2016.02.014.

[14] Y. Kawahito, K. Nakada, Y. Uemura, M. Mizutani, K. Nishimoto, H. Kawakami, S. Katayama, Relationship between melt flows based on three-dimensional X-ray transmission in situ observation and spatter reduction by angle of incidence and defocussing distance in high-power laser welding of stainless steel, Weld. Int. 32 (2018) 485–496. doi:10.1080/01431161.2017.1346887.

[15] P. Yuan, D. Gu, Molten pool behaviour and its physical mechanism during selective laser melting of TiC/AlSi10Mg nanocomposites: simulation and experiments, J. Phys. D. Appl. Phys. 48 (2015) 035303. doi:10.1088/0022-3727/48/3/035303.

[16] A. Matsunawa, J.-D. Kim, N. Seto, M. Mizutani, S. Katayama, Dynamics of keyhole and molten pool in laser welding, J. Laser Appl. 10 (1998) 247–254. doi:10.2351/1.521858.

[17] M. Xia, D. Gu, G. Yu, D. Dai, H. Chen, Q. Shi, Selective laser melting 3D printing of Ni-based superalloy: understanding thermodynamic mechanisms, Sci. Bull. 61 (2016) 1013–1022. doi:10.1007/s11434-016-1098-7.

[18] M. Sohail, S.-W. Han, S.-J. Na, A. Gumenyuk, M. Rethmeier, Characteristics of weld pool behavior in laser welding with various power inputs, Weld. World. 58 (2014) 269–277. doi:10.1007/s40194-014-0112-4.

[19] Z. Gan, G. Yu, X. He, S. Li, Surface-active element transport and its effect on liquid metal flow in laser-assisted additive manufacturing, Int. Commun. Heat Mass Transf. 86 (2017) 206–214. doi:10.1016/j.icheatmasstransfer.2017.06.007.

[20] S.K. Rauniyar, K. Chou, Melt pool analysis and mesoscale simulation of laser powder bed fusion process (L-PBF) with Ti-6Al-4V powder particles, JOM. 71 (2019) 938–945. doi:10.1007/s11837-018-3208-2.

[21] K. Abderrazak, S. Bannour, H. Mhiri, G. Lepalec, M. Autric, Numerical and experimental study of molten pool formation during continuous laser welding of AZ91 magnesium alloy, Comput. Mater. Sci. 44 (2009) 858–866. doi:10.1016/j.commatsci.2008.06.002.

[22] M. Courtois, M. Carin, P. Le Masson, S. Gaied, A two-dimensional axially-symmetric model of keyhole and melt pool dynamics during spot laser welding, Rev. Métallurgie. 110 (2013) 165–173. doi:10.1051/metal/2013060.

[23] M. Bachmann, V. Avilov, A. Gumenyuk, M. Rethmeier, About the influence of a steady magnetic field on weld pool dynamics in partial penetration high power laser beam welding of thick aluminium parts, Int. J. Heat Mass Transf. 60 (2013) 309–321. doi:10.1016/j.ijheatmasstransfer.2013.01.015.

[24] L. Zhang, J. Zhang, G. Zhang, W. Bo, S. Gong, An investigation on the effects of side assisting gas flow and metallic vapour jet on the stability of keyhole and molten pool during laser full-penetration welding, J. Phys. D. Appl. Phys. 44 (2011) 135201. doi:10.1088/0022-3727/44/13/135201.

[25] T. Zhang, H. Li, S. Liu, S. Shen, H. Xie, W. Shi, G. Zhang, B. Shen, L. Chen, B. Xiao, M. Wei, Evolution of molten pool during selective laser melting of Ti–6Al–4V, J. Phys. D. Appl. Phys. 52 (2019) 055302. doi:10.1088/1361-6463/aaee04.

[26] J. Peng, L. Li, S. Lin, F. Zhang, Q. Pan, S. Katayama, High-speed x-ray transmission and numerical study of melt flows inside the molten pool during laser welding of aluminum alloy, Math. Probl. Eng. 2016 (2016) 1–13. doi:10.1155/2016/1409872.

[27] N. Kouraytem, X. Li, R. Cunningham, C. Zhao, N. Parab, T. Sun, A.D. Rollett, A.D. Spear, W. Tan, Effect of laser-matter interaction on molten pool flow and keyhole

dynamics, Phys. Rev. Appl. 11 (2019) 064054. doi:10.1103/PhysRevApplied.11.064054.

[28] P. Jin, Z. Wenjie, W. Xingxing, G. Guoquan, Z. Furong, Numerical simulation of effect of filler wire melting and filling mode on molten pool in laser welding, Infrared Laser Eng. 47 (2018) 306005. doi:10.3788/IRLA201847.0306005.

[29] M. Xia, D. Gu, G. Yu, D. Dai, H. Chen, Q. Shi, Porosity evolution and its thermodynamic mechanism of randomly packed powder-bed during selective laser melting of Inconel 718 alloy, Int. J. Mach. Tools Manuf. 116 (2017) 96–106. doi:10.1016/j.ijmachtools.2017.01.005.

[30] H. Nakamura, Y. Kawahito, K. Nishimoto, S. Katayama, Elucidation of melt flows and spatter formation mechanisms during high power laser welding of pure titanium, J. Laser Appl. 27 (2015) 032012. doi:10.2351/1.4922383.

[31] M. Courtois, M. Carin, P. Le Masson, S. Gaied, M. Balabane, Guidelines in the experimental validation of a 3D heat and fluid flow model of keyhole laser welding, J. Phys. D. Appl. Phys. 49 (2016) 155503. doi:10.1088/0022-3727/49/15/155503.

[32] M. Schaefer, S. Kessler, F. Fetzer, T. Graf, Influence of the focal position on the melt flow during laser welding of steel, J. Laser Appl. 29 (2017) 012010. doi:10.2351/1.4972098.

[33] A. Matsunawa, N. Seto, M. Mizutani, S. Katayama, Liquid motion in keyhole laser welding, in: Int. Congr. Appl. Lasers Electro-Optics, Laser Institute of America, 1998: pp. G151–G160. doi:10.2351/1.5059193.

[34] F. Wirth, S. Arpagaus, K. Wegener, Analysis of melt pool dynamics in laser cladding and direct metal deposition by automated high-speed camera image evaluation, Addit. Manuf.

21 (2018) 369–382. doi:10.1016/j.addma.2018.03.025.

[35] H. Wang, M. Nakanishi, Y. Kawahito, Dynamic balance of heat and mass in high power density laser welding, Opt Express. 26 (2018) 6392–6399. doi:10.1364/OE.26.006392.

[36] Y. Naito, M. Mizutani, S. Katayama, Effect of oxygen in ambient atmosphere on penetration characteristics in single yttrium–aluminum–garnet laser and hybrid welding, J. Laser Appl. 18 (2006) 21–27. doi:10.2351/1.2164484.

[37] S. Katayama, Y. Kobayashi, M. Mizutani, A. Matsunawa, Effect of vacuum on penetration and defects in laser welding, J. Laser Appl. 13 (2001) 187–192. doi:10.2351/1.1404413.

[38] L. Aucott, H. Dong, W. Mirihanage, R. Atwood, A. Kidess, S. Gao, S. Wen, J. Marsden, S. Feng, M. Tong, T. Connolley, M. Drakopoulos, C.R. Kleijn, I.M. Richardson, D.J. Browne, R.H. Mathiesen, H. V Atkinson, Revealing internal flow behaviour in arc welding and additive manufacturing of metals, Nat. Commun. 9 (2018) 5414. doi:10.1038/s41467-018-07900-9.

[39] Q. Guo, C. Zhao, L.I. Escano, Z. Young, L. Xiong, K. Fezzaa, W. Everhart, B. Brown, T. Sun, L. Chen, Transient dynamics of powder spattering in laser powder bed fusion additive manufacturing process revealed by in-situ high-speed high-energy x-ray imaging, Acta Mater. 151 (2018) 169–180. doi:10.1016/j.actamat.2018.03.036.

[40] L.I. Escano, N.D.N.D. Parab, L. Xiong, Q. Guo, C. Zhao, K. Fezzaa, W. Everhart, T. Sun, L. Chen, Revealing particle-scale powder spreading dynamics in powder-bed-based additive manufacturing process by high-speed x-ray imaging, Sci. Rep. 8 (2018) 15079. doi:10.1038/s41598-018-33376-0.

[41] C.L.A. Leung, S. Marussi, M. Towrie, R.C. Atwood, P.J. Withers, P.D. Lee, The effect of powder oxidation on defect formation in laser additive manufacturing, Acta Mater. 166 (2019) 294–305. doi:https://doi.org/10.1016/j.actamat.2018.12.027.

[42] C. Zhao, K. Fezzaa, R.W. Cunningham, H. Wen, F. De Carlo, L. Chen, A.D. Rollett, T. Sun, Real-time monitoring of laser powder bed fusion process using high-speed X-ray imaging and diffraction, Sci. Rep. 7 (2017) 3602. doi:10.1038/s41598-017-03761-2.

[43] C.L.A. Leung, S. Marussi, R.C. Atwood, M. Towrie, P.J. Withers, P.D. Lee, In situ X-ray imaging of defect and molten pool dynamics in laser additive manufacturing, Nat. Commun. 9 (2018) 1355. doi:10.1038/s41467-018-03734-7.

[44] N.P. Calta, J. Wang, A.M. Kiss, A.A. Martin, P.J. Depond, G.M. Guss, V. Thampy, A.Y. Fong, J.N. Weker, K.H. Stone, C.J. Tassone, M.J. Kramer, M.F. Toney, A. Van Buuren, M.J. Matthews, An instrument for in situ time-resolved X-ray imaging and diffraction of laser powder bed fusion additive manufacturing processes, Rev. Sci. Instrum. 89 (2018) 55101. doi:10.1063/1.5017236.

[45] S.J. Wolff, H. Wu, N. Parab, C. Zhao, K.F. Ehmann, T. Sun, J. Cao, In-situ high-speed X-ray imaging of piezo-driven directed energy deposition additive manufacturing, Sci. Rep. 9 (2019) 962. doi:10.1038/s41598-018-36678-5.

[46] R. Cunningham, C. Zhao, N. Parab, C. Kantzos, J. Pauza, K. Fezzaa, T. Sun, A.D. Rollett, Keyhole threshold and morphology in laser melting revealed by ultrahigh-speed x-ray imaging, Science. 363 (2019) 849–852. doi:10.1126/science.aav4687.

[47] A.A. Martin, N.P. Calta, S.A. Khairallah, J. Wang, P.J. Depond, A.Y. Fong, V. Thampy, G.M. Guss, A.M. Kiss, K.H. Stone, C.J. Tassone, J. Nelson Weker, M.F. Toney, T. van

Buuren, M.J. Matthews, Dynamics of pore formation during laser powder bed fusion additive manufacturing, Nat. Commun. 10 (2019) 1987. doi:10.1038/s41467-019-10009-2.

[48] C. Kenel, D. Grolimund, X. Li, E. Panepucci, V.A. Samson, D.F. Sanchez, F. Marone, C. Leinenbach, In situ investigation of phase transformations in Ti-6Al-4V under additive manufacturing conditions combining laser melting and high-speed micro-X-ray diffraction, Sci. Rep. 7 (2017) 16358. doi:10.1038/s41598-017-16760-0.

[49] C. Kenel, D. Grolimund, J.L. Fife, V.A. Samson, S. Van Petegem, H. Van Swygenhoven, C. Leinenbach, Combined in situ synchrotron micro X-ray diffraction and high-speed imaging on rapidly heated and solidified Ti–48Al under additive manufacturing conditions, Scr. Mater. 114 (2016) 117–120. doi:10.1016/j.scriptamat.2015.12.009.

[50] R.W. Messler Jr, Principles of Welding, Wiley-VCH Verlag GmbH, Weinheim, Germany, 1999. doi:10.1002/9783527617487.

[51] S. Kou, C. Limmaneevichitr, P.S. Wei, Oscillatory Marangoni flow: a fundamental study by conduction-mode laser spot welding, Weld. J. 90 (2011) 229–240.

[52] M. Poletto, D.D. Joseph, Effective density and viscosity of a suspension, J. Rheol. (N. Y. N. Y). 39 (1995) 323–343. doi:10.1122/1.550692.

[53] P. Jin, H. Sumeng, W. Xingxing, W. Jiansheng, Z. Furong, Effect of filler metal on three-dimensional transient behavior of keyholes and molten pools in laser welding, Chinese J. Lasers. 45 (2018) 0102003. doi:10.3788/CJL201845.0102003.

[54] A. Paul, T. Debroy, Free surface flow and heat transfer in conduction mode laser welding,

Metall. Trans. B. 19 (1988) 851–858. doi:10.1007/BF02651409.

[55] P. Bidare, I. Bitharas, R.M. Ward, M.M. Attallah, A.J. Moore, Fluid and particle dynamics in laser powder bed fusion, Acta Mater. 142 (2018) 107–120. doi:10.1016/j.actamat.2017.09.051.

[56] B. Schoinochoritis, D. Chantzis, K. Salonitis, Simulation of metallic powder bed additive manufacturing processes with the finite element method: A critical review, Proc. Inst. Mech. Eng. Part B: J. Eng. Manuf. 231 (2017) 96–117. doi:10.1177/0954405414567522.

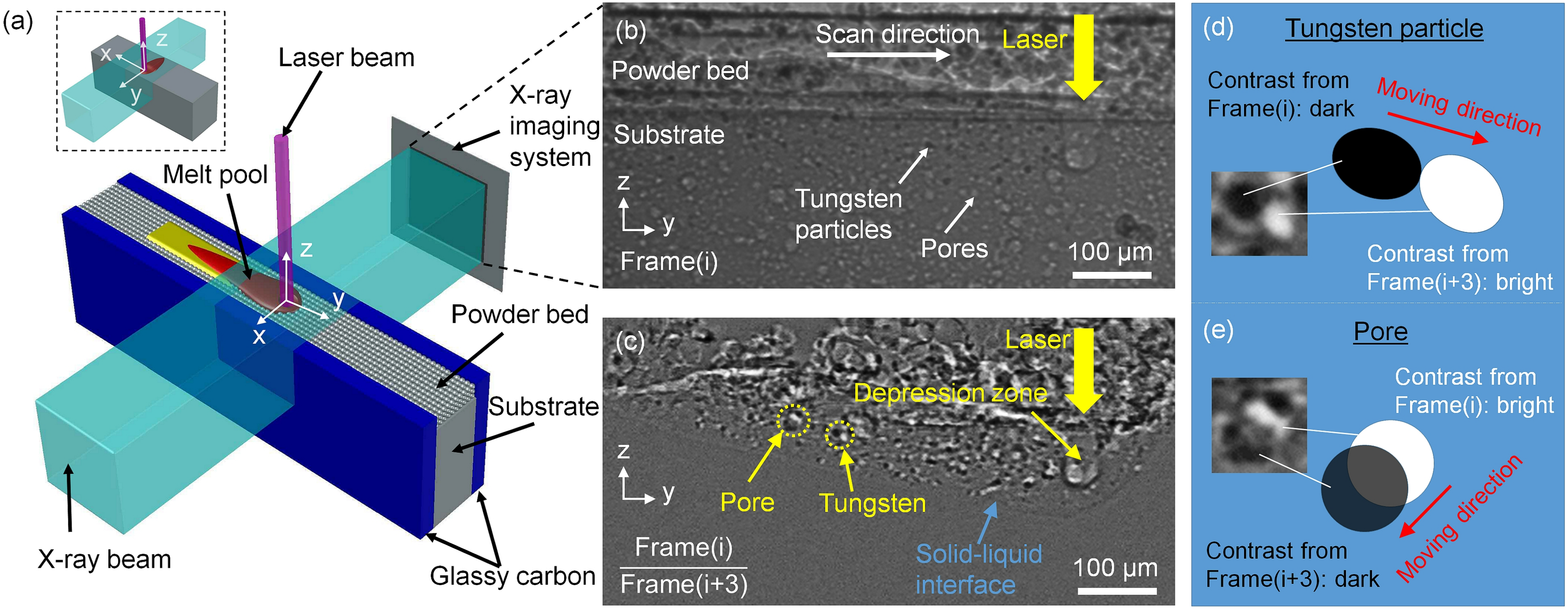
(a)
x
z
y
Laser beam
X-ray
imaging
system
Melt pool
z
y
x
Powder bed
Substrate
X-ray beam
Glassy carbon
(b)
Powder bed
Scan direction
Laser
Substrate
z
y
Tungsten
particles
Pores
Frame(i)
100 μm
(c)
Laser
Depression zone
z
y
Pore
Tungsten
Solid-liquid
interface
Frame(i)
Frame(i+3)
100 μm
(d)
Tungsten particle
Contrast from
Frame(i): dark
Moving direction
Contrast from
Frame(i+3): bright
(e)
Pore
Contrast from
Frame(i): bright
Contrast from
Frame(i+3): dark
Moving direction

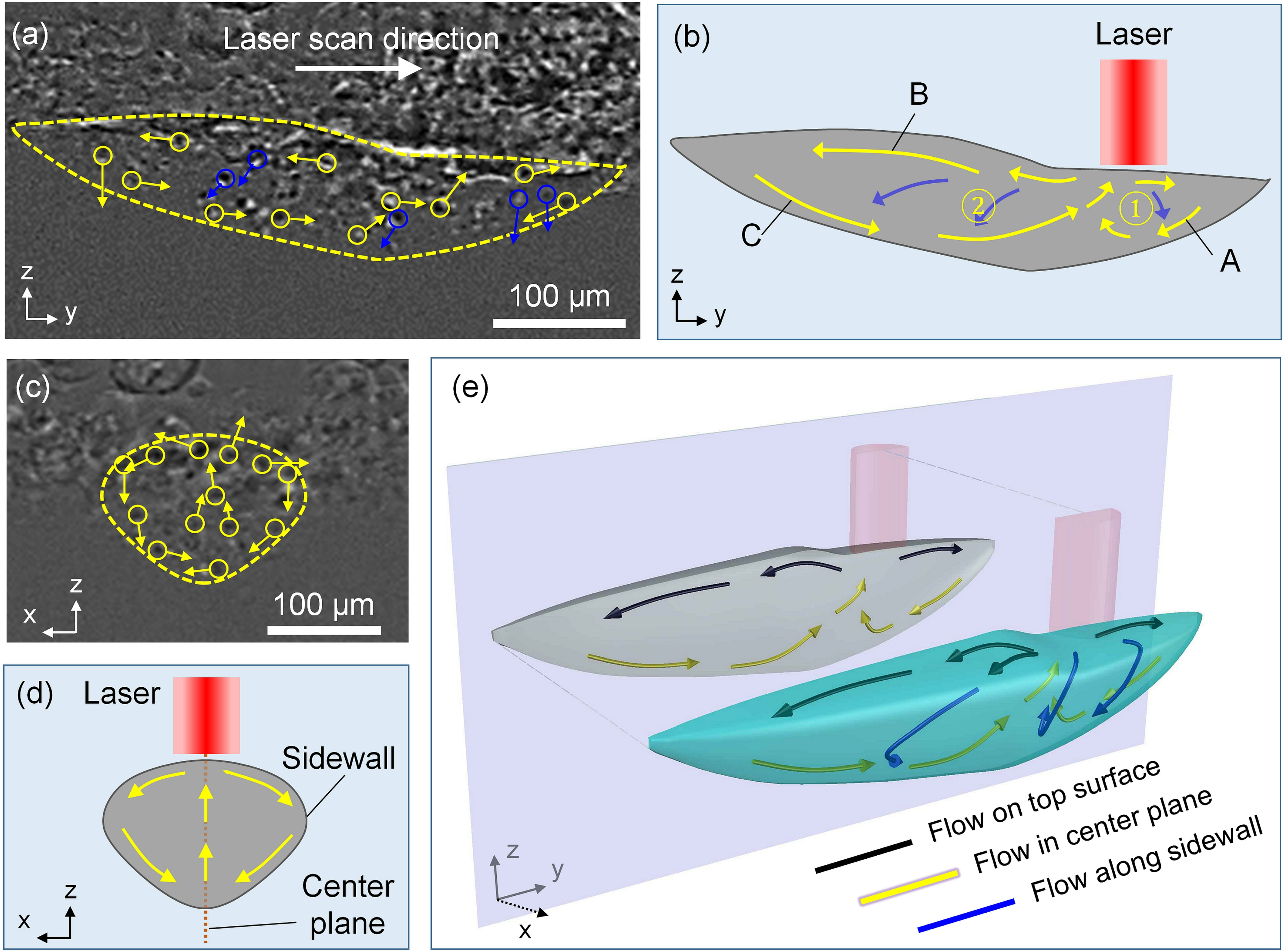
(a)
Laser scan direction
z
y
100 µm
(b)
Laser
B
C
②
①
A
z
y
(c)
z
x
100 µm
(d)
Laser
Sidewall
Center plane
z
x
(e)
z
y
x
Flow on top surface
Flow in center plane
Flow along sidewall

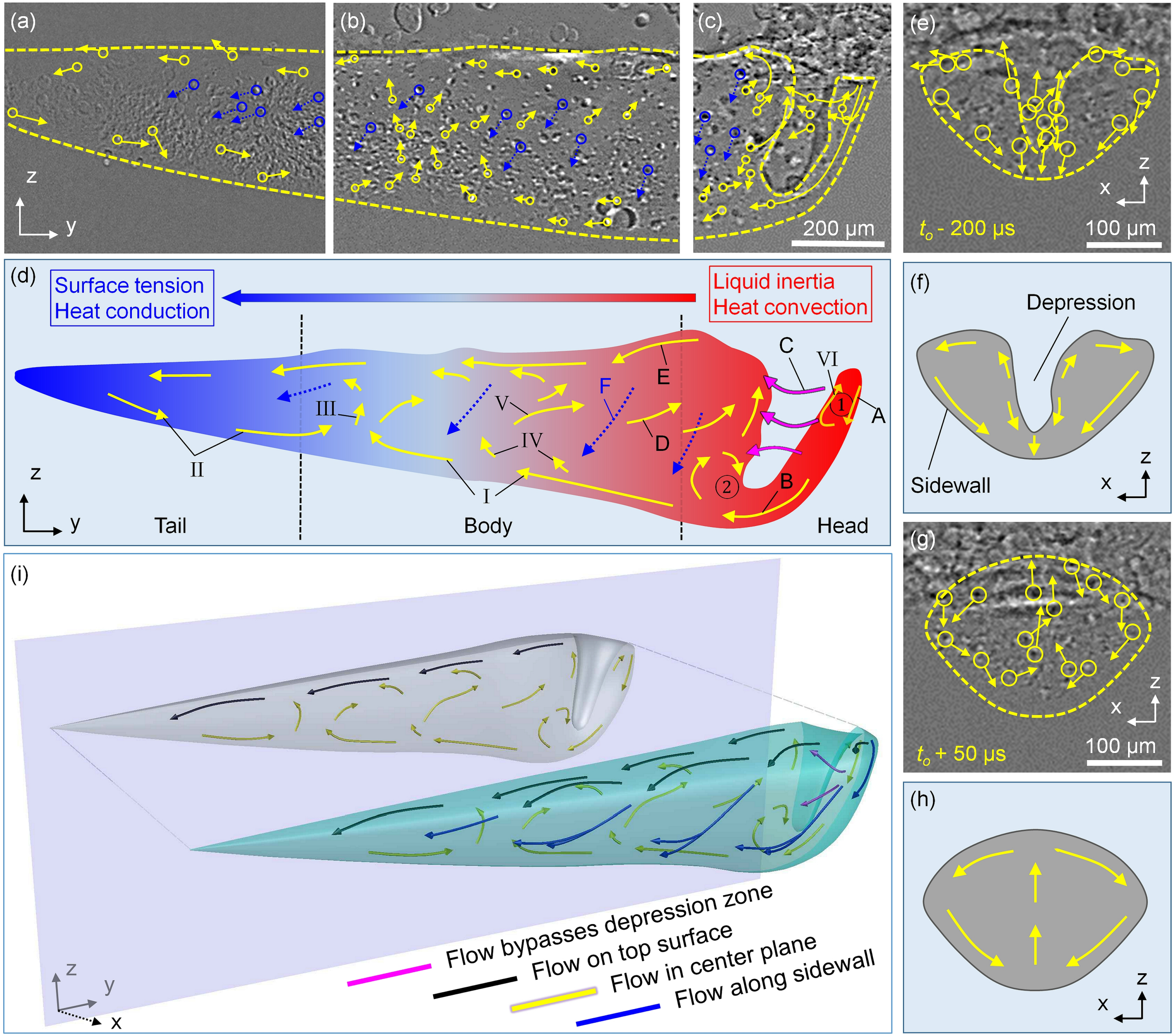
(a)
z
y
(b)
(c)
200 μm
(e)
z
x
t_o - 200 μs
100 μm
(d)
Surface tension
Heat conduction
Liquid inertia
Heat convection
C
VI
A
E
F
V
III
IV
II
D
B
①
②
I
z
y
Tail
Body
Head
(f)
Depression
Sidewall
z
x
(g)
z
x
t_o + 50 μs
100 μm
(h)
z
x
(i)
Flow bypasses depression zone
Flow on top surface
Flow in center plane
Flow along sidewall
z
y
x

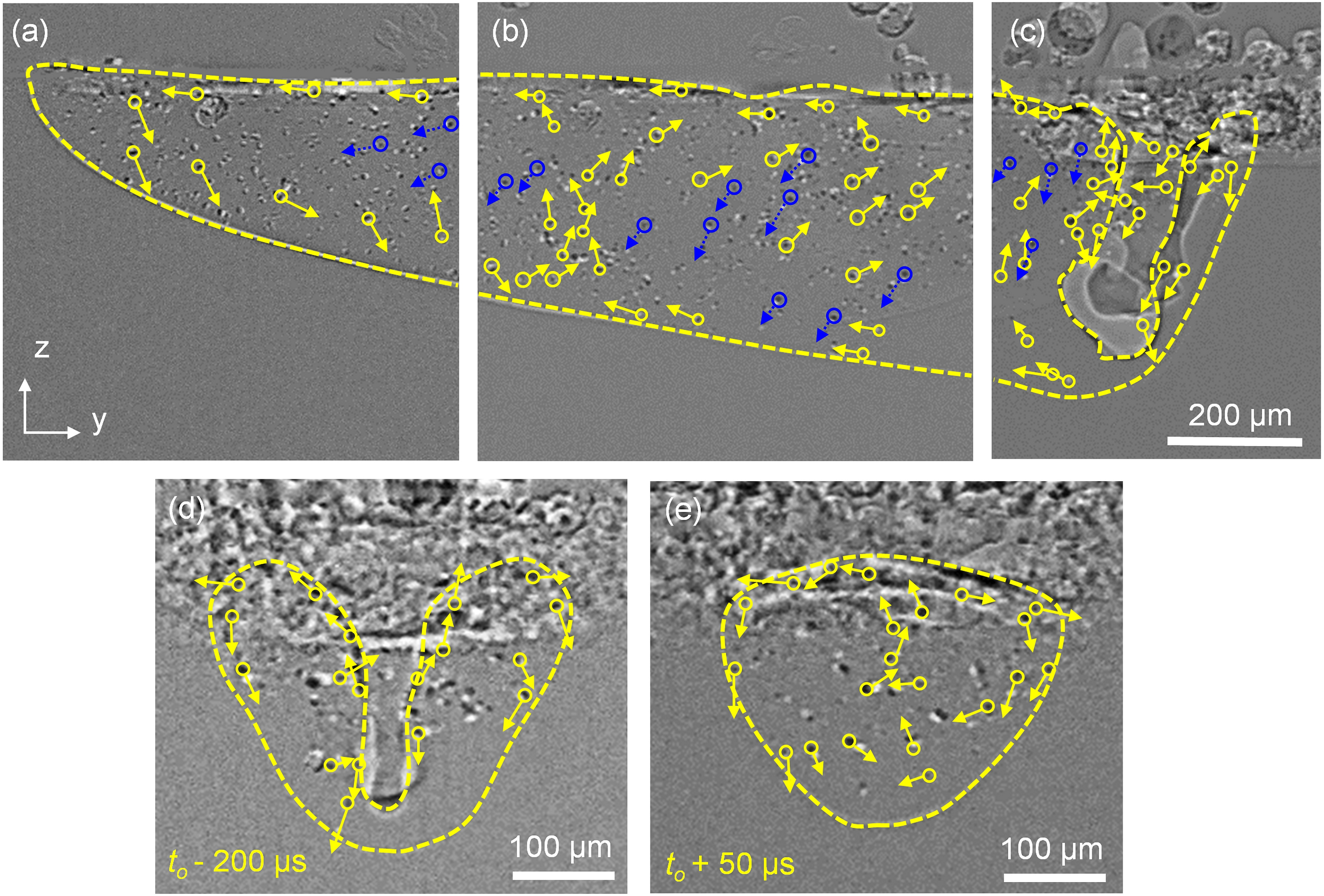
(a)
(b)
(c)
z
y
200 µm
(d)
(e)
t_o - 200 µs
100 µm
t_o + 50 µs
100 µm

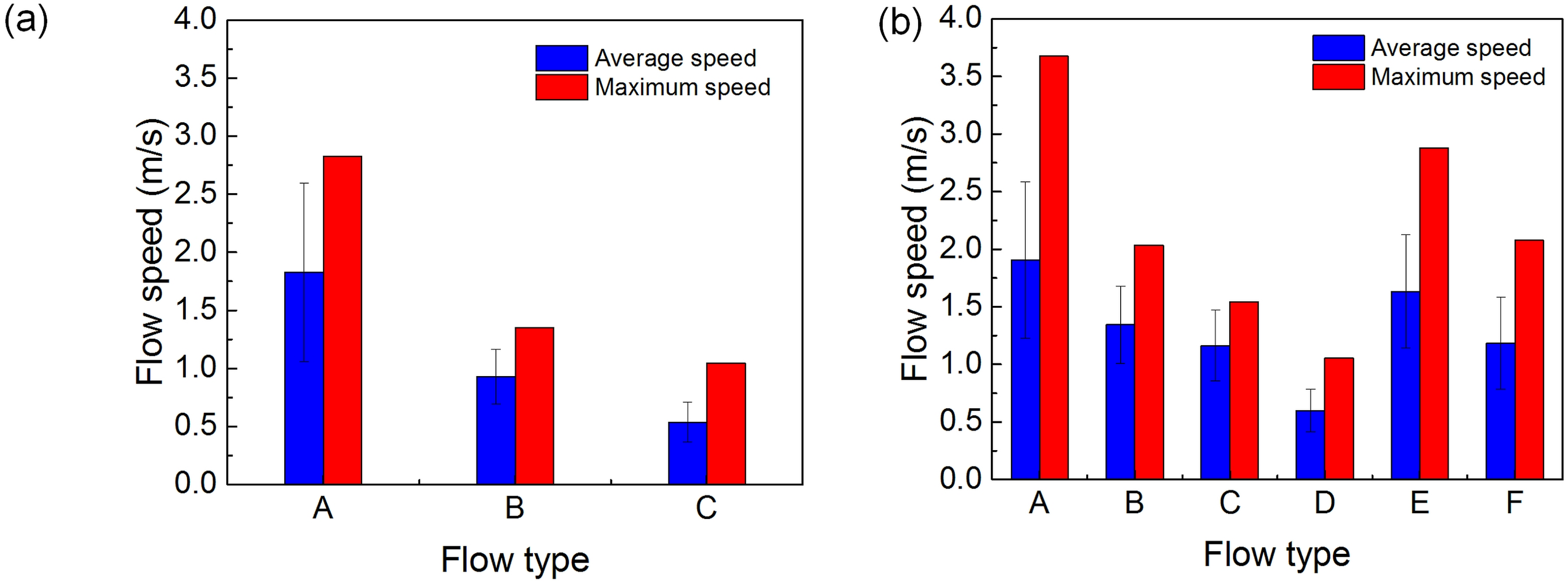
(a)
Flow speed (m/s)
0.0
0.5
1.0
1.5
2.0
2.5
3.0
3.5
4.0
Average speed
Maximum speed
A
B
C
Flow type
(b)
Flow speed (m/s)
0.0
0.5
1.0
1.5
2.0
2.5
3.0
3.5
4.0
Average speed
Maximum speed
A
B
C
D
E
F
Flow type

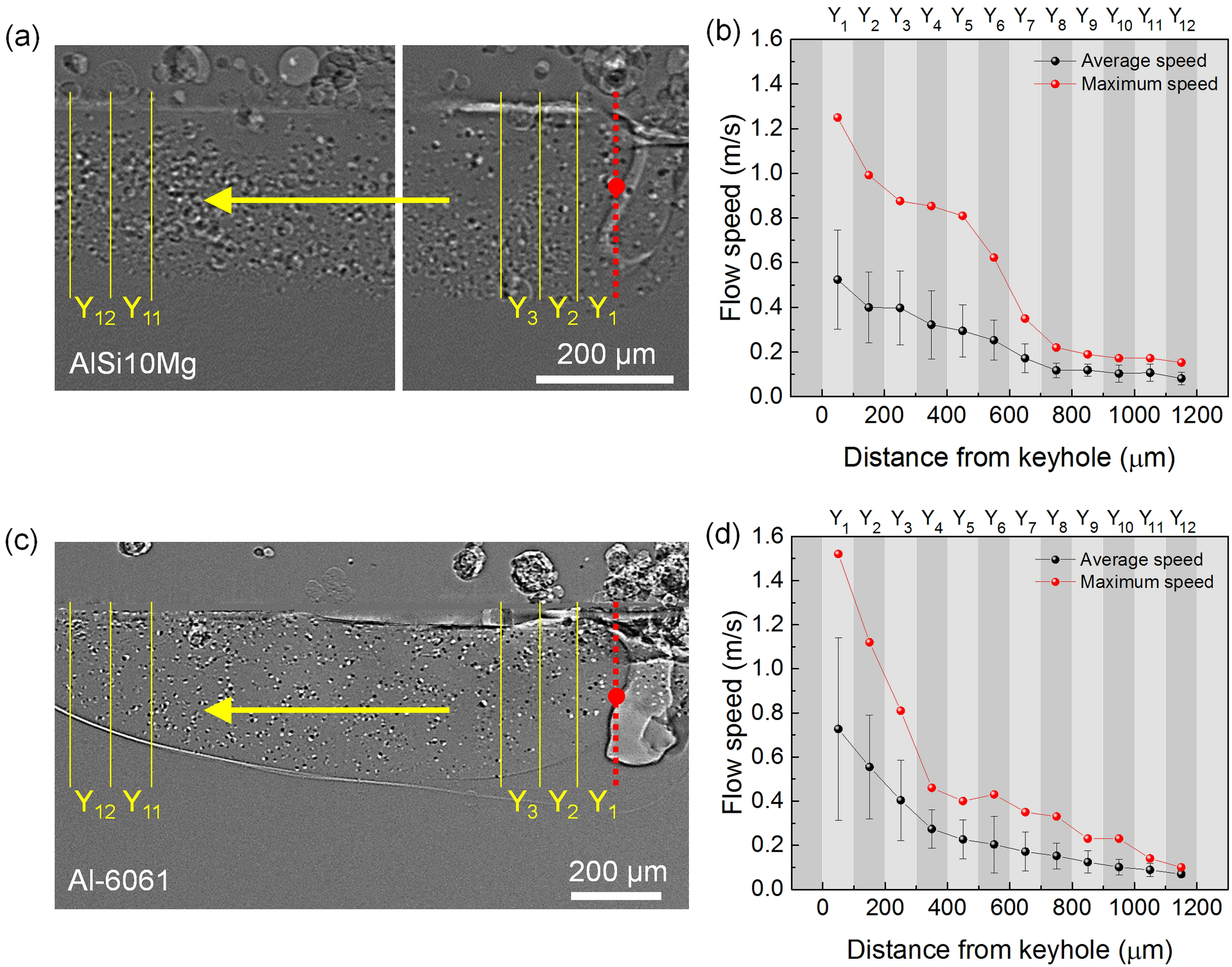
(a)
Y12 Y11
Y3 Y2 Y1
AlSi10Mg
200 μm
(b)
Y1 Y2 Y3 Y4 Y5 Y6 Y7 Y8 Y9 Y10 Y11 Y12
Average speed
Maximum speed
Flow speed (m/s)
0.0 0.2 0.4 0.6 0.8 1.0 1.2 1.4 1.6
0 200 400 600 800 1000 1200
Distance from keyhole (μm)
(c)
Y12 Y11
Y3 Y2 Y1
Al-6061
200 μm
(d)
Y1 Y2 Y3 Y4 Y5 Y6 Y7 Y8 Y9 Y10 Y11 Y12
Average speed
Maximum speed
Flow speed (m/s)
0.0 0.2 0.4 0.6 0.8 1.0 1.2 1.4 1.6
0 200 400 600 800 1000 1200
Distance from keyhole (μm)

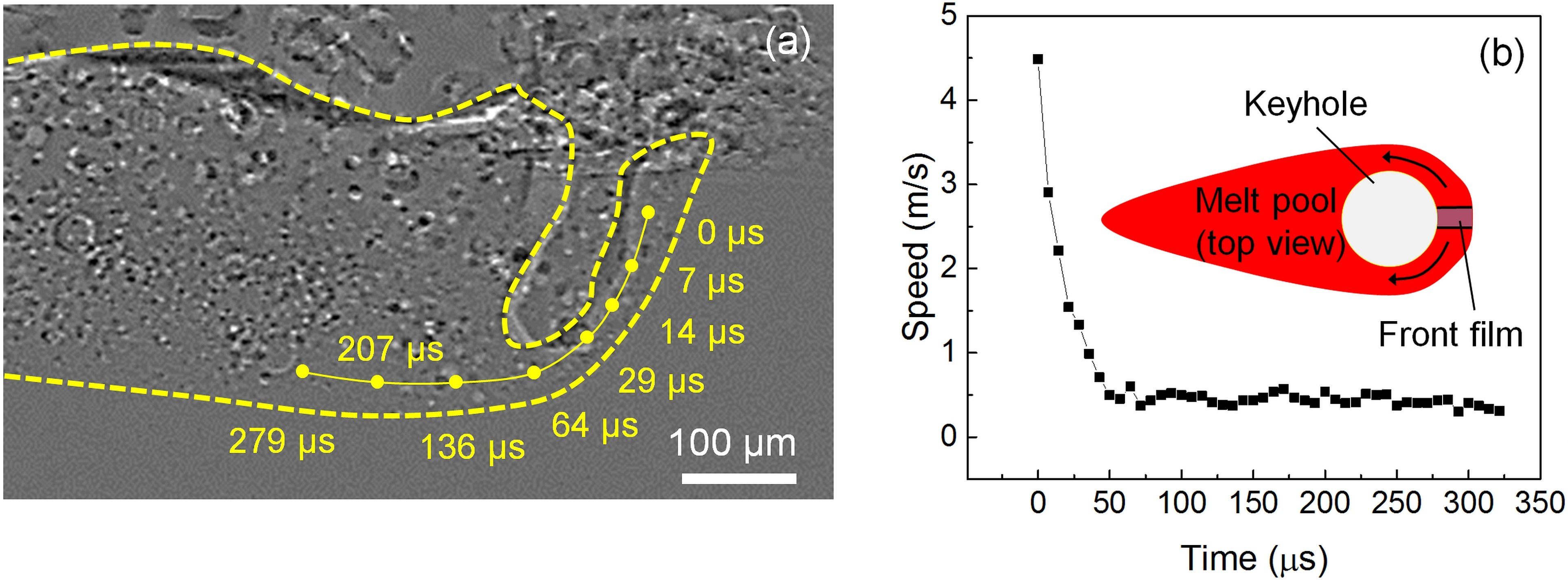
(a)
0 µs
7 µs
14 µs
29 µs
64 µs
136 µs
207 µs
279 µs
100 µm
(b)
Keyhole
Melt pool
(top view)
Front film
Speed (m/s)
Time (µs)
0
1
2
3
4
5
0
50
100
150
200
250
300
350

Table 1 Main processing parameters

Material	**Processing parameter**	**Melting mode**
AlSi10Mg	260 W, 0.6 m/s	Conduction mode
AlSi10Mg	364 W, 0.6 m/s	Depression mode
Al-6061	520 W, 0.4 m/s	Depression mode

Table 2 Types of flow and their locations

Melting mode	Flow type	Flow direction	Flow location
Conduction	**A**	Backward	Along the front melt pool bottom
	B	Backward	Along the melt pool surface
	C	Forward	Along the rear melt pool bottom
Depression	**A**	Downward	Along the front depression wall
	B	Downward & backward	Along the depression bottom
	C	Backward	Around the depression zone
	D	Upward & forward	Toward the depression outlet
	E	Backward	Along the surface of melt pool
	F	Downward & backward	Along the sidewall of melt pool

Declaration of Competing Interest

The authors declare that there is no conflict of interests.

Supplementary Materials for

In-situ full-field mapping of melt flow dynamics in laser metal additive manufacturing

Qilin Guo [a, b], Cang Zhao [c], Minglei Qu [a, b], Lianghua Xiong [b], S. Mohammad H. Hojjatzadeh [a, b], Luis I. Escano [a, b], Niranjan D. Parab [c], Kamel Fezzaa [c], Tao Sun [c, *], Lianyi Chen [a, b, **]

[a] Department of Mechanical Engineering, University of Wisconsin-Madison, Madison, WI 53706, USA

[b] Department of Mechanical and Aerospace Engineering, Missouri University of Science and Technology, Rolla, MO 65409, USA

[c] X-ray Science Division, Advanced Photon Source, Argonne National Laboratory, Lemont, IL 60439, USA

* Corresponding author

** Corresponding author

E-mail addresses: lianyi.chen@wisc.edu (Lianyi Chen), taosun@aps.anl.gov (Tao Sun)

Supplementary Figure 1

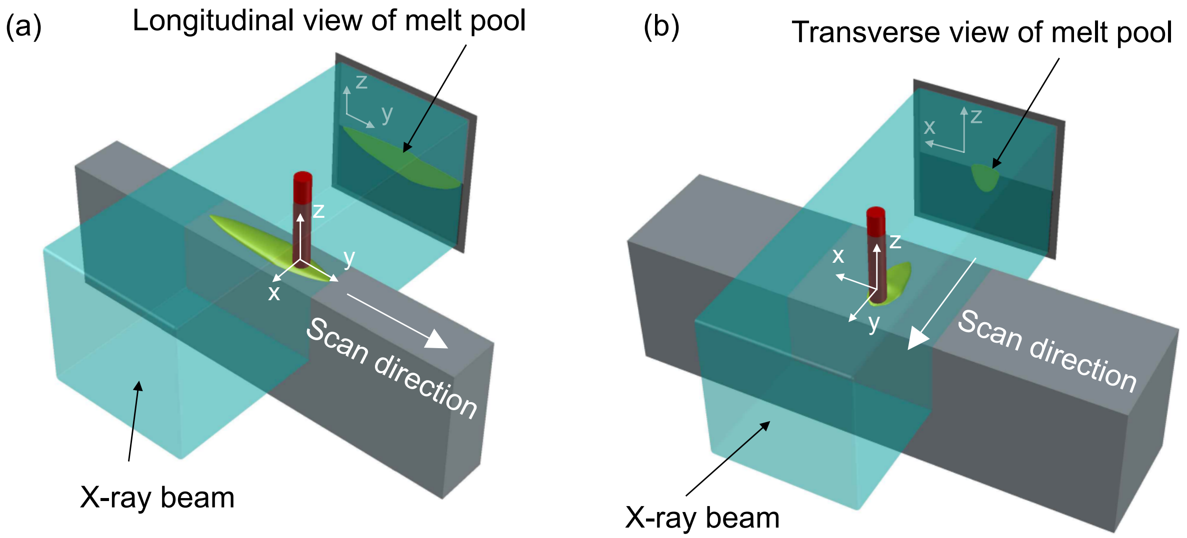

Supplementary Fig. 1. Schematics showing how the melt pool is projected onto the (a) y-z plane (longitudinal view) and (b) x-z plane (transverse view). Note that the powder bed and glassy carbon are not displayed in the drawing. The z direction is normal to the sample surface. The y direction is the laser scan direction. The x direction is normal to the y-z plane, following the right-hand rule. The thickness of substrate is 0.5 mm when the laser scan direction is perpendicular to the x-ray beam. The thickness of substrate is 1.0 mm when the laser scan direction is parallel to the x-ray beam.

Supplementary Movies

Supplementary Movie 1 Conduction-mode flow pattern transition between longitudinal and transverse view.

Supplementary Movie 2 Three-dimensional reconstruction of conduction-mode flow pattern in the whole melt pool.

Supplementary Movie 3 Depression-mode flow pattern (around depression) transition between longitudinal and transverse view.

Supplementary Movie 4 Depression-mode flow pattern (behind depression) transition between longitudinal and transverse view.

Supplementary Movie 5 Three-dimensional reconstruction of depression-mode flow pattern in the whole melt pool.

Supplementary Notes

Supplementary Note 1: Calculation of settling velocity

The settling velocity (v_p) of tungsten particle in liquid AlSi10Mg was calculated by the Stokes's law as

$$v_p = \frac{\rho_p - \rho_f}{\gamma \mu_f} g d_p^2 \tag{1}$$

where, g is the gravitational acceleration, d_p is the diameter of the particle, ρ_p is the mass density of the particle, ρ_f is the mass density of the fluid, μ_f is the dynamic viscosity of the fluid, γ is a coefficient which depends on the fluid and particle viscosity: $\gamma = 12[(\mu_f + \frac{3}{2}\mu_p)/(\mu_f + \mu_p)]$. $\gamma = 18$ in the case of solid particles ($\mu_p = \infty$). Take $g = 9.8$ m s^{-2}, $d_p = 5\times10^{-6}$ m, $\rho_p = 19{,}300$ kg m^{-3}, $\rho_f =$ 2,440 kg m^{-3} (at $T_m = 870$ K), $\mu_f = 0.00175$ kg m^{-1} s^{-1}), the settling velocity is calculated to be $v_p =$ 1.3×10^{-4} m s^{-1}.

Supplementary Note 2: Calculation of drag force and the iteration of tracer acceleration

Assuming the particle was accelerated from the top surface at the depression front (with an initial speed of 0 m/s) to the position marked by 0 μs (with a speed of 4.5 m s^{-1}) within one frame (7 μs), the maximum acceleration can be calculated as 6.4×10^5 m s^{-2}, which is equivalent to a force of 0.81 μN by Newton's second law. Given the driving force of the particle is the drag force by the molten aluminum, the drag force was calculated by the Schiller-Naumann drag law [1] as

$$F_d = \frac{3m_p}{4d_p} C_D v^2 \tag{2}$$

where, m_p is the particle mass, d_p is the particle diameter, v is the relative velocity, C_D is the Schiller-Naumann drag coefficient, which is given by

$$C_D = \frac{24}{Re_p}(1 + 0.15Re^{0.687}_p) \tag{3}$$

where the particle Reynolds number is $Re_p = \rho d_p v/\mu$, with the viscosity μ. Take $v = 4.5$ m s^{-1}, $\rho =$ 1,740 kg m^{-3} (near $T_b = 2{,}743$ K), $\mu = 0.0004$ kg m^{-1} s^{-1}) (near $T_b = 2{,}743$ K), the drag force was calculated to be $F_d = 4.2$ μN.

Consider that the drag force will decrease when the speed difference between the tracer and the flow becomes smaller, the total acceleration time can be estimated by iteration with small time steps. Assuming the initial tracer speed is zero, the surrounding flow speed is 4.5 m s^{-1} and the iteration time step is 1×10^{-8} s, it was calculated that the tungsten particle can be accelerated to over 50% of the surrounding flow speed within 1.4 μs. Furthermore, within one frame (~7 μs), the tracer speed can be accelerated to over 85% of the flow speed.

Supplementary Note 3: Calculation of viscosity of the mixed suspension

The viscosity (μ_m) of the mixed suspension (liquid AlSi10Mg + solid tungsten) was calculated by [2]

$$\mu_m = \mu_f(1 + 2.5\phi + 10.05\phi^2) \tag{4}$$

where ϕ is the solid fraction. Taking $\phi = 0.01$, the mixture viscosity is calculated to be $\mu_m = 1.026\mu_f$.

Supplementary Note 4: Details about Marangoni force

Marangoni effect is one of the major driving forces acting in the melt pool [3–6]. A dimensionless number, Marangoni number (Ma), is often used to evaluate the relative effect of Marangoni flow over liquid viscosity [7] as

$$Ma = -\frac{d\sigma}{dT}\cdot\frac{L\Delta T}{\mu\alpha} \tag{5}$$

where $d\sigma/dT$ = -0.31×10^{-4} N m^{-1} K^{-1} is the surface tension coefficient for AlSi10Mg alloy, L = 2.0 mm is the length of the melt pool, $\Delta T = T_b - T_m$ = 1,873 K, $\mu_{1000\,K}$ = 0.014 (g cm^{-1} s^{-1}) is the dynamic viscosity of the liquid AlSi10Mg, and α_{1000K} = 4×10^{-5} m^2 s^{-1} is the thermal diffusivity of liquid AlSi10Mg. The Marangoni number in AlSi10Mg melt pool is calculated to be Ma = 2,074, indicating a strong Marangoni flow. Physically, a Marangoni flow occurs in liquid with a surface tension gradient induced by the temperature gradient as well as concentration gradient, as descried by [8]

$$\frac{\partial\sigma}{\partial T} =- A - R\Gamma_s \ln\left(1 + K\alpha_s\right) - \frac{K\alpha_s\Gamma_s\Delta H_0}{T(1 + K\alpha_s)} \tag{6}$$

and

$$K = k_1 \exp\left(-\frac{\Delta H_0}{RT}\right) \tag{7}$$

where A is the absolute value of the surface tension temperature coefficient, R is the universal gas constant, Γ_s is the surface excess at saturation, k_1 is a constant related to the segregation entropy, ΔH_0 is the standard heat of adsorption, α_s is the activity of an active element. Since there is usually no surface active agent in aluminum alloys [9], the surface tension coefficient is always negative ($\partial\sigma/\partial T < 0$) in the present work, which means the Marangoni flow in the melt pool is temperature-dependent, thus has a trend of moving from the hotter region to cooler region. A flow driven purely by thermal gradient is also called thermocapillary flow. The typical feature of Marangoni flow in a melt pool is the outward flow at the laser heating spot, i.e., the surface flow ahead of laser beam moves forward while the surface flow behind the laser beam moves backward. However, extra attention must be paid to the following circumstances: adding surface active agents [8,10–13] , applying high-speed shielding/carrier gas directly to the melt pool (such as DED additive manufacturing) [14], changing processing atmosphere [1,11,15–17], and applying electromagnetic field (such as laser-arc hybrid melting) [9,11,18]. These operations can potentially reverse the direction of thermal-induced Marangoni flow completely.

Supplementary Note 5: Details about vaporization induced forces

Vaporization is another major driving force for liquid flow in laser melting [19–21], particularly under depression mode in which strong vaporization occurs. In fact, vaporization has two simultaneous, yet different, effects on the depression zone: the recoil pressure pushing the liquid downward [22,23], and the upward metallic vapor plume sprouting out of the depression outlet [5,24]. Consequently, the flow around the lower part of the depression zone tends to move down, while the flow near the upper depression-zone walls tends to move up [10,20,23]. Vaporization is an important factor that accounts for some defects in laser-processed part. For instance, the excess recoil pressure can change the local curvature of the depression zone and generate pores in the melt pool [25]; also, the high-speed vapor plume may interact with the depression-zone rim and shear off droplets out of melt pool as spatters [26].

Supplementary Note 6: Details about hydraulic pressure

The effect of hydraulic pressure includes the hydrostatic pressure and hydrodynamic pressure. Assuming the liquid is incompressible and the variation of gravitational acceleration is negligible (g = constant), the hydraulic pressure can be approximated by [27]

$$P_h = P_{static} + P_{dynamic} = \rho g \Delta h + \frac{1}{2}\rho v^2 \tag{8}$$

where Δh is the depth of the test area from the reference position, v is the fluid velocity. Since the hydraulic pressure is determined by the position and the velocity of the flow, it plays important roles in the following events: (1) evacuating the fluid out of the liquid film ahead of the depression,

(2) rebounding the flow at the melt pool boundary, (3) changing the flow direction by dragging the fluid into low hydraulic pressure region, (4) exchanging momentum when two flows encounter each other.

Supplementary Note 7: Details about buoyancy force

The density of liquid metal varies with temperature. In a melt pool, the buoyancy force (B) is a function of density gradient [21,27,28] as

$$B = \rho g \beta \Delta T \tag{9}$$

where β is the thermal expansion coefficient, ΔT is the temperature difference among the convective liquid flow. Generally, the effect of buoyance force is believed to be less significant than the Marangoni force in laser processing [1,24]. The dynamic Bond number (Bo) [7] can be used to assess the relative effectiveness of buoyance force and Marangoni force as

$$Bo = \frac{\rho g \beta L^2}{d\sigma/dT} \tag{10}$$

Taking $\beta = 2\times10^{-4}$ K^{-1} for liquid AlSi10Mg, the dynamic Bond number is estimated to be $Bo \approx 0.1$, which indicates the density effect is less than the surface tension effect. However, the buoyance force does play a role in the melt pool in the case where the hot liquid entering the melt pool bottom and floating up [29]. The buoyance force may also participate in assisting the upward flow along the upper depression-zone walls [18], but the contribution may be small compared with the strong effect of vapor plume.

Supplementary Note 8: Calculation of hydraulic diameter

Hydraulic diameter is commonly used to describe flow moving through non-circular pipes or channels. It is defined by:

$$D_h = \frac{4A}{P_w} \tag{11}$$

where A is the cross section area of the flow, and the P_w is the wetted perimeter of the cross section.

Considering the melt pool as a channel with a cross section shape of half ellipse, one radius of the ellipse is the melt pool depth, while the other radius is half of the melt pool width. In Fig. 6(a), section Y_1, the melt pool depth is 313 µm, with a width of ~500 µm. The hydraulic diameter is calculated to be 539 µm. In the section Y_{12} of Fig. 6(a), the melt pool depth is 248 µm with a width of 396 µm. The hydraulic diameter is calculated to be 427 µm.

References

[1] F. Wirth, S. Arpagaus, K. Wegener, Analysis of melt pool dynamics in laser cladding and direct metal deposition by automated high-speed camera image evaluation, Addit. Manuf. 21 (2018) 369–382. doi:10.1016/j.addma.2018.03.025.

[2] M. Poletto, D.D. Joseph, Effective density and viscosity of a suspension, J. Rheol. (N. Y. N. Y). 39 (1995) 323–343. doi:10.1122/1.550692.

[3] F. Tenner, B. Berg, C. Brock, F. Klämpfl, M. Schmidt, Experimental approach for quantification of fluid dynamics in laser metal welding, J. Laser Appl. 27 (2015) S29003. doi:10.2351/1.4906302.

[4] K. Abderrazak, S. Bannour, H. Mhiri, G. Lepalec, M. Autric, Numerical and experimental study of molten pool formation during continuous laser welding of AZ91 magnesium alloy, Comput. Mater. Sci. 44 (2009) 858–866. doi:10.1016/j.commatsci.2008.06.002.

[5] P. Jin, H. Sumeng, W. Xingxing, W. Jiansheng, Z. Furong, Effect of filler metal on three-dimensional transient behavior of keyholes and molten pools in laser welding, Chinese J. Lasers. 45 (2018) 0102003. doi:10.3788/CJL201845.0102003.

[6] A. Paul, T. Debroy, Free surface flow and heat transfer in conduction mode laser welding, Metall. Trans. B. 19 (1988) 851–858. doi:10.1007/BF02651409.

[7] Z.S. Saldi, Marangoni driven free surface flows in liquid weld pools, Delft University of Technology, 2012. doi:https://doi.org/10.4233/uuid:8401374b-9e9c-4d25-86b7-fc445ec73d27.

[8] Z. Gan, G. Yu, X. He, S. Li, Surface-active element transport and its effect on liquid metal flow in laser-assisted additive manufacturing, Int. Commun. Heat Mass Transf. 86 (2017) 206–214. doi:10.1016/j.icheatmasstransfer.2017.06.007.

[9] S. Kou, Y.H. Wang, Computer simulation of convection in moving arc weld pools, Metall. Trans. A. 17 (1986) 2271–2277. doi:10.1007/BF02645925.

[10] Y. Kawahito, Y. Uemura, Y. Doi, M. Mizutani, K. Nishimoto, H. Kawakami, M. Tanaka, H. Fujii, K. Nakata, S. Katayama, Elucidation of the effect of welding speed on melt flows in high-brightness and high-power laser welding of stainless steel on basis of three-dimensional X-ray transmission in situ observation, Weld. Int. 31 (2017) 206–213. doi:10.1080/09507116.2016.1223204.

[11] Y. Naito, M. Mizutani, S. Katayama, Effect of oxygen in ambient atmosphere on penetration characteristics in single yttrium–aluminum–garnet laser and hybrid welding, J. Laser Appl. 18 (2006) 21–27. doi:10.2351/1.2164484.

[12] S. Kou, C. Limmaneevichitr, P.S. Wei, Oscillatory Marangoni flow: a fundamental study by conduction-mode laser spot welding, Weld. J. 90 (2011) 229–240.

[13] L. Aucott, H. Dong, W. Mirihanage, R. Atwood, A. Kidess, S. Gao, S. Wen, J. Marsden, S. Feng, M. Tong, T. Connolley, M. Drakopoulos, C.R. Kleijn, I.M. Richardson, D.J. Browne, R.H. Mathiesen, H. V Atkinson, Revealing internal flow behaviour in arc welding and additive manufacturing of metals, Nat. Commun. 9 (2018) 5414. doi:10.1038/s41467-018-07900-9.

[14] L. Zhang, J. Zhang, G. Zhang, W. Bo, S. Gong, An investigation on the effects of side assisting gas flow and metallic vapour jet on the stability of keyhole and molten pool during laser full-penetration welding, J. Phys. D. Appl. Phys. 44 (2011) 135201. doi:10.1088/0022-3727/44/13/135201.

[15] A. Matsunawa, J.-D. Kim, N. Seto, M. Mizutani, S. Katayama, Dynamics of keyhole and molten pool in laser welding, J. Laser Appl. 10 (1998) 247–254. doi:10.2351/1.521858.

[16] S. Katayama, Y. Kobayashi, M. Mizutani, A. Matsunawa, Effect of vacuum on penetration and defects in laser welding, J. Laser Appl. 13 (2001) 187–192. doi:10.2351/1.1404413.

[17] M. Schaefer, S. Kessler, F. Fetzer, T. Graf, Influence of the focal position on the melt flow during laser welding of steel, J. Laser Appl. 29 (2017) 012010. doi:10.2351/1.4972098.

[18] M. Bachmann, V. Avilov, A. Gumenyuk, M. Rethmeier, About the influence of a steady magnetic field on weld pool dynamics in partial penetration high power laser beam welding of thick aluminium parts, Int. J. Heat Mass Transf. 60 (2013) 309–321. doi:10.1016/j.ijheatmasstransfer.2013.01.015.

[19] Y. Zhao, Y. Koizumi, K. Aoyagi, D. Wei, K. Yamanaka, A. Chiba, Molten pool behavior and effect of fluid flow on solidification conditions in selective electron beam melting (SEBM) of a biomedical Co-Cr-Mo alloy, Addit. Manuf. 26 (2019) 202–214. doi:10.1016/j.addma.2018.12.002.

[20] S.A. Khairallah, A.T. Anderson, A. Rubenchik, W.E. King, Laser powder-bed fusion additive manufacturing: Physics of complex melt flow and formation mechanisms of pores, spatter, and denudation zones, Acta Mater. 108 (2016) 36–45. doi:10.1016/j.actamat.2016.02.014.

[21] M. Sohail, S.-W. Han, S.-J. Na, A. Gumenyuk, M. Rethmeier, Characteristics of weld pool behavior in laser welding with various power inputs, Weld. World. 58 (2014) 269–277. doi:10.1007/s40194-014-0112-4.

[22] I. Eriksson, J. Powell, A.F.H. Kaplan, Melt behavior on the keyhole front during high speed laser welding, Opt. Lasers Eng. 51 (2013) 735–740. doi:10.1016/j.optlaseng.2013.01.008.

[23] H. Nakamura, Y. Kawahito, K. Nishimoto, S. Katayama, Elucidation of melt flows and spatter formation mechanisms during high power laser welding of pure titanium, J. Laser Appl. 27 (2015) 032012. doi:10.2351/1.4922383.

[24] A. Matsunawa, N. Seto, M. Mizutani, S. Katayama, Liquid motion in keyhole laser welding, in: Int. Congr. Appl. Lasers Electro-Optics, Laser Institute of America, 1998: pp. G151–G160. doi:10.2351/1.5059193.

[25] S. Katayama, Y. Kawahito, M. Mizutani, Elucidation of laser welding phenomena and factors affecting weld penetration and welding defects, Phys. Procedia. 5 (2010) 9–17.

doi:10.1016/j.phpro.2010.08.024.

[26] Y. Kawahito, K. Nakada, Y. Uemura, M. Mizutani, K. Nishimoto, H. Kawakami, S. Katayama, Relationship between melt flows based on three-dimensional X-ray transmission in situ observation and spatter reduction by angle of incidence and defocussing distance in high-power laser welding of stainless steel, Weld. Int. 32 (2018) 485–496. doi:10.1080/01431161.2017.1346887.

[27] B. Chang, C. Allen, J. Blackburn, P. Hilton, D. Du, Fluid flow characteristics and porosity behavior in full penetration laser welding of a titanium alloy, Metall. Mater. Trans. B. 46 (2015) 906–918. doi:10.1007/s11663-014-0242-5.

[28] J. Peng, L. Li, S. Lin, F. Zhang, Q. Pan, S. Katayama, High-speed x-ray transmission and numerical study of melt flows inside the molten pool during laser welding of aluminum alloy, Math. Probl. Eng. 2016 (2016) 1–13. doi:10.1155/2016/1409872.

[29] M. Xia, D. Gu, G. Yu, D. Dai, H. Chen, Q. Shi, Selective laser melting 3D printing of Ni-based superalloy: understanding thermodynamic mechanisms, Sci. Bull. 61 (2016) 1013–1022. doi:10.1007/s11434-016-1098-7.